European Journal of Medicinal Chemistry 254 (2023) 115386

Contents lists available at ScienceDirect

European Journal of Medicinal Chemistry

journal homepage: www.elsevier.com/locate/ejmech

Research paper

Neurotensin(8–13) analogs as dual NTS1 and NTS2 receptor ligands with enhanced effects on a mouse model of Parkinson's disease

Toni Kühl [a], Maya G. Georgieva [b], Harald Hübner [c], Maria Lazarova [d], Matthias Vogel [e], Bodo Haas [e], Martina I. Peeva [b], Aneliya A. Balacheva [b], Ivan P. Bogdanov [b], Luigi Milella [f], Maria Ponticelli [f], Tsvetomir Garev [g], Immacolata Faraone [f,h], Roumyana Detcheva [b], Borislav Minchev [d], Polina Petkova-Kirova [d], Lyubka Tancheva [d,i], Reni Kalfin [d], Atanas G. Atanasov [j,k], Liudmil Antonov [l], Tamara I. Pajpanova [b], Kiril Kirilov [b,m], Marcus Gastreich [n], Peter Gmeiner [c], Diana Imhof [a], Nikolay T. Tzvetkov [b,*]

[a] Pharmaceutical Biochemistry and Bioanalytics, Pharmaceutical Institute, University of Bonn, An der Immenburg 4, D-53121, Bonn, Germany
[b] Department of Biochemical Pharmacology and Drug Design, Institute of Molecular Biology "Roumen Tsanev", Bulgarian Academy of Sciences, Acad. G. Bonchev Str., bl. 21, Sofia, 1113, Bulgaria
[c] Department of Chemistry and Pharmacy, Medicinal Chemistry, Friedrich-Alexander- Universität Erlangen-Nürnberg, Nikolaus-Fiebiger-Str. 10, D-91058, Erlangen, Germany
[d] Institute of Neurobiology, Bulgarian Academy of Sciences, Acad. G. Bonchev Str., bl. 23, 1113, Sofia, Bulgaria
[e] Federal Institute for Drugs and Medical Devices (BfArM), Kurt-Georg-Kiesinger-Allee 3, 53175, Bonn, Germany
[f] Department of Science, University of Basilicata, V.le dell'Ateneo Lucano 10, 85100, Potenza, Italy
[g] UMBALSM "N. I. Pirogov"-Hospital, 1606 Pette Kyosheta, Sofia, Bulgaria
[h] Innovative Startup Farmis s.r.l., Via Nicola Vaccaro 40, 85100, Potenza, Italy
[i] Weizmann Institute of Science, 234 Herzl St., Rehovot, 7610001, Israel
[j] Ludwig Boltzmann Institute for Digital Health and Patient Safety, Medical University of Vienna, Spitalgasse 23, 1090, Vienna, Austria
[k] Institute of Genetics and Animal Biotechnology of the Polish Academy of Sciences, Jastrzebiec, 05-552, Magdalenka, Poland
[l] Institute of Electronics, Bulgarian Academy of Sciences, Blvd. Tsarigradsko Chaussee 72, 1784, Sofia, Bulgaria
[m] Department of Natural Sciences, New Bulgarian University, 21 Montevideo Str., Sofia, 1618, Bulgaria
[n] BioSolveIT GmbH, An der Ziegelei 79, 53757 St. Augustin, Germany

ARTICLE INFO

Keywords:
Neurotensin
Peptide analogs
Agonists
Neurotensin receptors
Parkinson's disease

ABSTRACT

The modulatory interactions between neurotensin (NT) and the dopaminergic neurotransmitter system in the brain suggest that NT may be associated with the progression of Parkinson's disease (PD). NT exerts its neurophysiological effects by interactions with the human NT receptors type 1 (hNTS1) and 2 (hNTS2). Therefore, both receptor subtypes are promising targets for the development of novel NT-based analogs for the treatment of PD. In this study, we used a virtually guided molecular modeling approach to predict the activity of NT(8–13) analogs by investigating the docking models of ligands designed for binding to the human NTS1 and NTS2 receptors. The importance of the residues at positions 8 and/or 9 for hNTS1 and hNTS2 receptor binding affinity was experimentally confirmed by radioligand binding assays. Further *in vitro* ADME profiling and *in vivo* studies revealed that, compared to the parent peptide NT(8–13), compound 10 exhibited improved stability and BBB permeability combined with a significant enhancement of the motor function and memory in a mouse model of PD. The herein reported NTS1/NTS2 dual-specific NT(8–13) analogs represent an attractive tool for the development of therapeutic strategies against PD and potentially other CNS disorders.

1. Introduction

Neurotensin (NT) is an endogenous tridecapeptide (pELYENKPRRPYIL-OH, pE: pyroGlu) that is widely expressed throughout the central nervous system (CNS) and periphery [1–3]. NT exerts its physiological functions as a neuromodulator or

* Corresponding author.
E-mail address: ntzvetkov@bio21.bas.bg (N.T. Tzvetkov).

https://doi.org/10.1016/j.ejmech.2023.115386
Received 4 March 2023; Received in revised form 15 April 2023; Accepted 16 April 2023
Available online 17 April 2023

neurotransmitter in the brain and as a paracrine-endocrine hormone, mainly in the gastrointestinal tract (GIT), but also in peripheral organs [1,4–6]. It shows a variety of biological effects and is involved in the pathogenesis of several conditions, many of them associated with the disturbance of regulatory functions of NT within the CNS and the GIT [5,8]. Indeed, NT plays an important role in the regulation of key physiological processes including hypothermia, hypotension, non-opioid analgesia, obesity, drug addiction, cancer-cell growth, regulation of neurotransmitter signaling, and others [2,5,7] [–] [10].

In the brain, NT is highly expressed in the amygdala, lateral septum, ventral tegmental area (VTA), and substantia nigra (SN), and thus, modulates neurotransmitter systems such as the dopaminergic, glutamatergic, GABAergic, cholinergic, and serotonergic systems [1,8,11–13]. The neurophysiological effects of NT are mediated by its interaction with two cell-membrane NT receptors (NTSRs), the NT receptor type 1 and 2 (NTS1R and NTS2R), both belonging to the family of G protein-coupled receptors (GPCRs) possessing seven transmembrane helices with 64% amino acid homology [4,8]. There are also two other NTRs that are expressed in the CNS, namely NTS3R/sortilin/gp95 (type I membrane glycoprotein Vps10p family sorting receptor) and NTS4R/SorLA/LR11 (yeast sorting sortilin related receptor), whose roles in mediating NT activity are so far not completely understood [1,12,14–16]. While the NTS1R is expressed also in the peripheral tissues (mostly in the GIT), the NTS2R is localized in the brain [1,7]. Thus, both NTS1R and NTS2R are responsible for the neurophysiological activity of NT with higher affinity for NTS1R over NTS2R [1,2,7,12].

In particular, NT modulates directly or indirectly (e.g., via glutamate release) dopamine (DA) neurotransmission through different neuronal mechanisms, including antagonistic NT/D_2 receptor interaction and second messenger-dependent receptor alteration [7,8,12,17]. The co-localization of NTS1 with both presynaptic and postsynaptic dopamine D_2 receptors (NTS1R/D_2R), especially within the nigrostriatal pathway, is an evidence of an allosteric receptor-receptor interaction [7,13]. In fact, the NT inhibition of presynaptic D_2 autoreceptors leads to an increase in DA levels, whereas the co-localization of NTS1R with postsynaptic DA receptors decreases the dopamine signal transduction [13,18]. Moreover, both NTS1 and NTS2 receptors are also found in high concentrations on dopaminergic neurons in the SN, suggesting that the activation of the NTRs in this region by NT may stimulate the DA release [7,18]. Accordingly, the main effect of NT binding in SN is a D_2 autoreceptor inhibition with a subsequent increase of DA signaling [7,18]. There are also *in vivo* studies showing that NT analogs may reduce Parkinsonian motor disfunctions and rigidity in rats, induced with 6-hydroxydopamine (6-OHDA) [19,20]. Therefore, both NTS1R and NTS2R represent attractive targets in the treatment of Parkinson's disease (PD), and possibly other neurodegenerative disorders.

In previous works, we used a rational drug design strategy in searching for favorable modifications on the NT(8–13) backbone in order to obtain analogs with improved stability as well as enhanced neuroprotective effects *in vivo* [19]. Herein, we used a molecular modeling approach to predict the activity of NT(8–13) analogs by investigating the docking models of single or double modified NT(8–13) analogs at the homology models of human NTS1 and NTS2 receptors. Based on virtually estimated dual NTS1R and NTS2R activity, we describe the synthesis, the structural characterization, and the experimental confirmation of compounds' affinities at both NTSRs by using radioligand binding assays. We further report functional, chemical and *in vitro* pharmacological studies leading to the development of compound **10** (Lys^8-Cav^9-Pro^{10}-Tyr^{11}-Ile^{12}-Leu^{13}), a full agonist of the NTS1 receptor with improved stability and permeability compared to the parent peptide NT(8–13). In addition, we further provide evidence on enhanced neuroprotective properties of **10** in various *in vivo* experiments using a murine model of PD as well as a lack of toxicity *in vitro*.

2. Results and discussion

2.1. Design of neurotensin analogs

Although the linear backbone of NT comprises a 13 amino acid sequence (**1**, Fig. 1A), its C-terminal hexapeptide NT(8–13) represents the pharmacologically active fragment sharing the common features for binding to NTS1R and NTS2R [21,22]. Both, NT and NT(8–13), are highly potent agonists that selectively bind to the NTS1 receptor with K_i values in the subnanomolar range [23]. Therefore, NT(8–13) is considered as a lead structure for the development of NT-based peptide and non-peptide analogs (agonists and antagonists) as potential therapeutic or imaging agents [23–28]. Due to the rapid degradation of NT *in vivo* by proteolytic cleavage of the bonds between Arg^8-Arg^9 (cleavage site c1), Pro^{10}-Tyr^{11} (c2) and Tyr^{11}-Ile^{12} (c3) [2,26,29], many synthetic strategies were focused on the development of NT(8–13)-based mimetics with improved stability, including linear [24–26] and macrocyclic analogs [30,31]. The majority of them has been developed either as NTS1R or NTS2R-selective ligands, e.g., as radiolabeled tools [24,27] or non-opioid analgesics with potential use in the management of acute and chronic pain [25,30–32]. To date, several synthetic strategies have been applied to increase binding affinity and NTS1R/NTS2R selectivity as well as to improve stability and other physicochemical parameters of NT(8–13) analogs.

For example, these approaches included replacement of the arginine residues in positions 8 and 9 by lysine leading to enhanced dual activity and retained selectivity of the resulting peptide **3** toward both receptor subtypes (strategy I, Fig. 1B) [25,33]. Further replacement of Tyr^{11} by lysine and of the C-terminal residue by (*L*)-(trimethylsilyl)alanine led to a 10-fold increase in hNTS2 selectivity and an improved stability (peptide **4**, cf. Fig. 1B) [25]. Recently, the crucial role of Tyr^{11} in hNTS1/hNTS2 selectivity and hNTS1 activation was further demonstrated by molecular dynamics simulations [34]. Another strategy to obtain stabilized NTS1-selective NT(8–13) analogs includes the substitution of Ile^{12} by *tert*-butylglycine (Tle) in ABS-201 (**5**, $C_\alpha$methyl-homolysine^8-Arg^9-Pro^{10}-Tyr^{11}-Tle^{12}-Leu^{13}), also known as KK13 or HPI-201 [23], followed by an *N*-methylation of Arg^8 (compound **6**) or Arg^9 (compound **7**) [26]. The peptidomimetic ABS-201 is a potent and selective NTS1R agonist able to cross the blood-brain barrier (BBB), and therefore, a promising drug candidate for the treatment of ischemic stroke and probably other traumatic injuries [2,35,36]. The N-methylated NT(8–13) analogs **6** and **7** exhibited highly improved enzymatic stability, which may be useful for the development of stable radiopharmaceuticals (strategy II, Fig. 1B) [26].

The majority of the so far reported synthetic strategies deal with hNTS1 [26,27,30,36] or hNTS2 [25,28,31,37,38] selective NT(8–13) analogs, but only few of them are focused on the exploration of dual NTS1/NTS2 acting NT(8–13) peptidomimetics, however, with modified C-terminal linear core structure [33]. Therefore, it would be of scientific interest to investigate the influence of specific amino acid residues at the N-terminal (e.g., positions 8 and/or 9) of the NT(8–13) fragment on permeability, stability, receptor binding affinity, and NTS1/NTS2 selectivity.

Based on earlier studies on the C-terminal hexapeptide NT(8–13) (**2**) representing the pharmacologically active fragment of NT (**1**, cf. Fig. 1), which selectively binds to both hNTS1R and hNTS2R [21–23,39–41], we intended to design new ligands based on structural analysis upon modification of positions 8 and/or 9 in the parent core structure, while retaining residues 10–13 (cf. Fig. S1).

2.2. Homology modeling of hNTRs

To virtually estimate the receptor affinity and hNTS1/hNTS2 selectivity of the NT(8–13) analogs intended for synthesis, molecular modeling and docking experiments were anticipated. However, in the absence of structural analyses of the human NTSR1/2 we first focused on

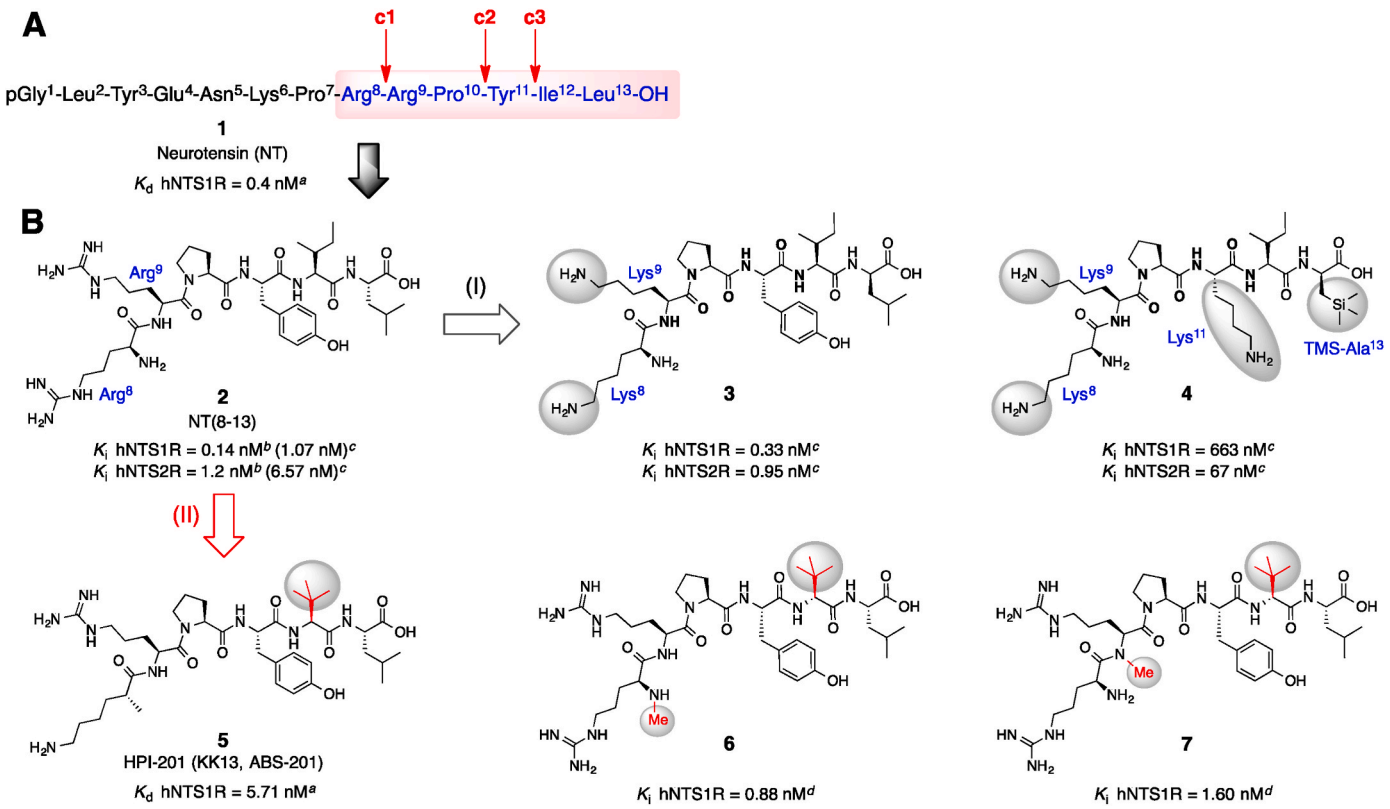

Fig. 1. Structures, reported hNTSRs affinities and strategies for the development of linear NT(8–13) (**2**) analogs. (A) Amino acid sequence of NT (**1**) and its biologically active fragment (NT aa sequence 8–13, in blue) with the major enzymatic cleavage sites (c1–c3, in red). (B) Chemical structures, reported binding affinities and intended synthetic strategies for the development of hNTS2R (strategy I) or hNTS1R selective (strategy II) agonists **3**–**7** derived from the parent structure NT (8–13) (**2**). The modified/introduced amino acid residues are indicated in blue (for I) or red (for II), while the performed structural modifications in comparison to **2** are remarked with grey ellipses (cf. I). The structural modifications leading to an improved human plasma stability (>86%, 48h for **6**; >99%, 48h for **7**)[d] are given in red und surrounded with grey ellipses (cf. II). [a]Ref. 23. [b]Ref. 24. [c]Ref. 25. [d]Ref. 26.

establishing homology models for both receptors based on existing structures of the rat NTSR1 in complex with NT(8–13) (PDB ID: 4GRV) (Supporting information, Fig. S2) [42–45].

Recently, cryo-EM structures of the human NTS1 receptor in complex with β-arrestins 1 and 2 or the agonist JMV449 and the heterotrimeric $G\alpha_{i1}$ protein have been reported [46–48]. This structural basis has therefore allowed us to obtain and optimize the 3D structures of both human NTS1 and NTS2 receptors by homology modeling (cf. Fig. S2).

In order to compare the homology models with the X-ray structure of rNTS1 in complex with NT(8–13), the 3D structures of the receptors were superimposed based on their N-terminal domains (Fig. S3). In fact, the rNTS1R and the homology models of hNTS1R and hNTS2R are almost identical in their extracellular part, consisting of three extracellular loops (ECL1-ECL3) and seven transmembrane α-helices (TM1-TM7) [42,45], and differ in the intracellular part. NT(8–13) (**2**) showed the same orientation within the binding pockets of the receptors (Fig. S3A) with the arginine residues at positions 8 and 9 pointing outwards the receptor surface, while the C-terminal of ligand **2** is oriented into the more lipophilic part inside the binding pocket (Figs. S3B and S3C) [30,42]. Important H-bonds were observed with residues Ser93, Tyr112, Arg316, Tyr320, Tyr336, and Trp 328 within the binding pocket of the rNTS1R. Overall, the superimposed models of the hNTS1 and hNTS2 receptors with rNTS1 reproduced the composition of the binding pocket for **2** in all three receptors [42,45]. We subsequently performed docking experiments with the intended NT(8–13) analogs (**10**–**14**, Scheme 1) at the homology models of both receptors using the SeeSAR package [49]. The results suggested that substitutions at Arg^8 and/or Arg^9 by Lys and/or Cav of the NT(8–13) backbone should lead to dually active analogs against hNTS1R and hNTS2R with estimated affinities in the nanomolar range, or potentially even better.

2.3. Synthesis and analysis of NT(8–13) analogs

Aiming to perform a systematic study on the biological effects and SARs resulting from the envisaged NT(8–13) (**2**) backbone modifications, peptide **2** and its analogs **10**–**14** including their precursor **9** were synthesized by standard solid-phase peptide synthesis (SPPS) according to the 9-fluorenylmethoxycarbonyl (Fmoc) protecting group strategy (Scheme 1) [39,41,50,51]. An automated SPPS continuous flow synthesizer, preloaded 2-chlorotrityl resin and HBTU as the coupling reagent were used to obtain resin-bound peptides **8b** and **8c**. Tetrapeptide **9** was prepared from **8c** after final cleavage from the resin and deprotection reaction. Peptide **8c** was further subjected to a two-step manual synthesis procedure to obtain **8d** by using HOBt/HBTU and DIEA for coupling of all Fmoc-amino acids. Fmoc-deprotection was performed with 20% piperidine in DMF. For final cleavage from the resin and removal of protecting groups, a TFA/reagent K mixture was used. All fully deprotected peptides were purified by semi-preparative RP-HPLC, affording compounds **2**, and **10**–**14** in good to high overall yields (Table S1). In accordance with our strategy, all synthesized peptides contained the same precursor sequence H-PYIL-OH (**9**), which was further included as a control in all biological studies in order to investigate the effects of positions 8 and 9 on the NTS1 and NTS2 receptor binding affinities.

Based on their structural similarity, the solution NMR structures of peptides **10** and **13** from the synthesized set were analyzed. Both peptides exhibit the same amino acid sequence at 9–13, but differ in their N-terminal amino acid (cf. Scheme 1). In addition, peptide **13** differs from

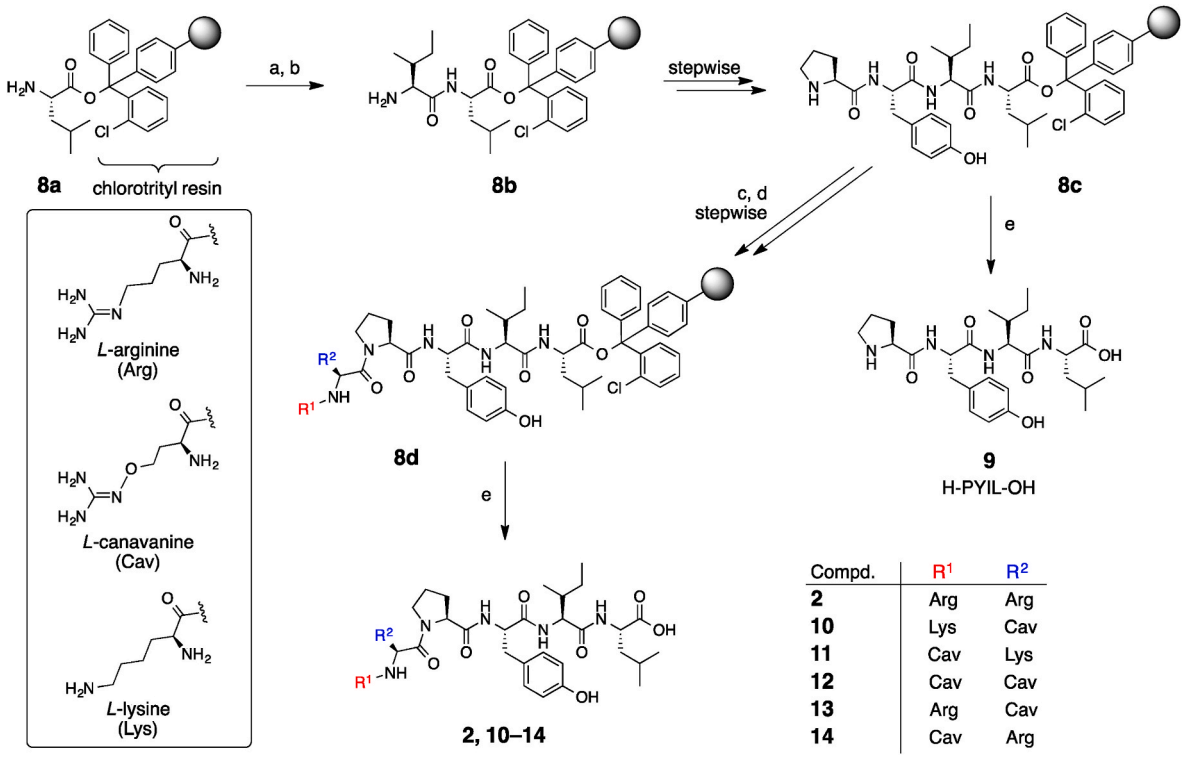

Scheme 1. Synthesis of tetrapeptide 9, NT(8–13) (2) and its analogs 10–14[a].

[a]Reagents and conditions: All reactions were carried out at room temperature. For steps (a) and (b) automated solid-phase peptide synthesis (SPPS) was applied using a continuous flow system. For reactions (c) and (d) a manual approach was chosen using batch methodology. (a) Fmoc-amino acid derivative (5.0 equiv.), HBTU (5.0 equiv.) in the presence of N-methyl-morpholine/DMF (1:1), 5–15 min; (b) 20% piperidine in DMF, 2 × 6 min; (c) Fmoc-amino acid derivative (4.0 equiv.), HBTU (4 equiv.), HOBt (4.0 equiv.), DIEA (8 equiv.), 1 × 30 min, 1 × 60 min – in case of coupling of Fmoc-Cav(Boc)-OH 2.0 equiv. were used in the first coupling and 1.0 equiv. in the second coupling and the other chemicals were scaled down accordingly; (d) 20% piperidine in DMF, 1 × 5 min, 1 × 15 min; (e) 1.0 mL/100 mg resin reagent K (75 mg phenol, 25 μL 1,2-ethandithiol, 50 μL thioanisol, 50 μL water in 1.0 mL TFA), 3 h, filtration and precipitation in cold diethyl ether.

the parent NT(8–13) core structure only at the amino acid residue at position 9, i.e., Cav instead of Arg. The same change was introduced at position 9 of peptide **10**. Thus, both peptides represent double (peptide **10**) or single (peptide **13**) modified analogs of the NT(8–13) core structure, respectively. The 3D solution structures of peptides **10** and **13** were determined using 2D-NMR spectroscopy, including 2D DQF-COSY, TOCSY and NOESY techniques (Table S2). Overall, the spectra displayed a high overlap in the core amino acids 10–13 (especially at Pro^{10} and Tyr^{11}), differing significantly in the orientation of the N-terminal residues, i.e. Lys^{8} (in **10**) or Arg^{8} (in **13**) as well as Cav^{9} for both analogs (Fig. 2). For peptide **10**, 46 NOEs were identified, whereas for its analog **13** altogether 31 NOEs were assigned (Table S3). All NOEs were used for structure calculation and excellent final Z-scores of 2.210 and 0.221 were achieved. The resulting 3D structures were highly flexible, with a backbone RMSD of 1.581 Å and 1.941 Å, respectively (cf. Table S3).

In order to investigate the most stable conformation within the top 20 estimated NMR poses (conformers) for peptides **10** and **13**, quantum-chemical calculations were performed at the neutral state of both peptides [53–55]. In fact, the results from these studies would reveal a deeper insight into the relationship between the bioactivity at the conformational ground state and the isomeric stability of the guanidine (Arg) and oxo-guanidine (Cav) group containing peptides **10** and **13**. Using a B3-LYP functional with defTZVP [56] basis set for the single point energy calculations in ground state, the theoretical experiments were carried out in water as a solvent by the use of implicit solvation model (for details, see Table S4 and Fig. S6) [57–59]. The

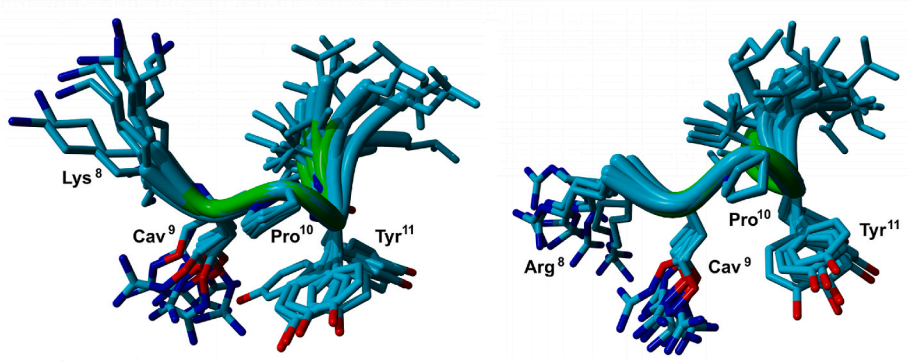

Fig. 2. NMR structures of NT-analogs **10** (left) and **13** (right). The solution NMR structures are presented as ensemble of the highest scoring 10 structures from the final ensemble. The NMR solve macro in YASARA (version 20.4.242) was used to calculate the peptide structures based on the chemical shifts data [52].

quantum-chemical calculations in water suggested that there is no conformational equilibrium for peptides **10** and **13**, which are positively charged under physiological conditions.

2.4. Binding affinity studies

Radioligand binding studies were carried out to evaluate parent peptide **2**, its analogs **10**–**14**, and the precursor peptide **9** (control) for their binding affinity toward both NTS1 and NTS2 receptors. Therefore, membranes from human embryonic kidney 293 (HEK293) cells transiently transfected with pcDNA3.1+ for hNTS1R or hNTS2R expression and the radioligand [Leu^{3}H]NT(8–13) as a radioactive reference were used [38,60–62]. To predict binding affinities at both NTSRs, the scoring function HYDE (HYdrogen DEsolvation) in SeeSAR was used [49]. HYDE rapidly computes estimations of binding affinities and delivers ranges of $K_{i\ HYDE}$ values (cf. Structural modeling section) [63–65]. The results from the radioligand binding experiments (expressed as K_i values) and the estimated HYDE binding affinities ranges as well as the hNTSRs selectivity (expressed as SI) are summarized in Table 1. In fact, double substitution of Arg^8/Arg^9 by Lys and/or Cav (peptides **10**–**12**) as well as single replacement of Arg^8 or Arg^9 by Cav (peptides **12** and **14**) in the NT (8–13) core structure resulted in an overall decrease in affinity and, with exception of **14**, in a loss of selectivity toward hNTS1R and hNTS2R compared to NT(8–13) (**2**, hNTS1: $K_i = 0.68 \pm 0.04$ nM and hNTS2: $K_i = 1.8 \pm 0.17$ nM). However, the NT(8–13) analogs **10**–**14** were found to be highly potent at both NTSRs with K_i values in the low nanomolar range (cf. Table 1).

Furthermore, the importance of positions 8 and 9 for high-affinity receptor binding was provided by control tetrapeptide **9** lacking the amino acids at both positions. Compound **9** showed a dramatic decrease in affinity at both receptors with $K_i > 50000$ nM for hNTS1 and hNTS2 compared to all tested peptides. This is an experimental evidence that amino acid residues at positions 8 and 9 in the NT(8–13) backbone are crucial for binding affinity. Moreover, the estimated affinity ranges (HYDE scores/$K_{i\ HYDE}$ in low nM) for peptides **10**–**14** as well as for **2** at both hNTS1R and hNTS2R are in good agreement with the experimental data from the radioligand binding assays (cf. Table 1). The observed decrease in binding affinities and reversed selectivity, e.g., from hNTS1-selective peptide **2** to dual-specific hNTS1/hNTS2-active analogs **10**–**14**, can tentatively be connected to the different orientation and conformations of the N-terminal residues, leading to less favorable interactions within ECL2 and/or ECL3 of both NTRs.

A double replacement of Arg^8 and Arg^9 by Lys^8/Cav^9 or Cav^8/Lys^9 in **2** resulted in compounds **10** and **11**, respectively. While peptide **10** showed a minor decrease in NTS1R and NTS2R affinity compared to **2** (**2** *vs.* **10**: $K_i = 0.68 \pm 0.04$ *vs.* 6.9 ± 0.59 nM toward hNTS1R and $K_i = 1.8 \pm 0.17$ *vs.* 6.5 ± 0.63 nM toward hNTS2R), compound **11** was found to be 2-fold less active at both human NTRs when compared to **10** (for **11**, K_i of 15 ± 4.5 and 14 ± 4.4 nM toward hNTS1R and hNTS2R, respectively). Both peptides **10** and **11** were equally selective at both NTRs with SI = 1.06 and 1.07, respectively. Thus, introduction of two Cav residues at positions 8 and 9, e.g., by replacement of Arg^8/Arg^9 by Cav^8/Cav^9 in **2**, led to a significant loss of affinity for compound **12** at hNTS1R ($K_i = 60 \pm 5.4$ nM) and hNTS2R ($K_i = 54 \pm 11$ nM), being >8- and ~4-fold less affine at both NTRs compared to peptide **10** and **11**, respectively. Considering the doubly modified NT(8–13) analogs **10**–**12** it can be concluded that a Cav residue at position 9 that mimics the guanidine function of Arg^9 and a lipophilic amino acid at the N-terminus of **2** (such as lysine in **10**) are still well-tolerated in terms of their receptor affinity.

Next, we evaluated the influence of single modifications with a positively charged residue in peptides **13** and **14**, where Arg^9 or Arg^8 were replaced by a canavanine. These modifications resulted in recovery of binding affinities at hNTS1R and hNTS2R comparable to these of **10**, however, with slightly decreased affinity when compared to the parent peptide **2** (cf. Table 1). Among the investigated set of NT(8–13) analogs, compound **13** was the most potent toward hNTS2R with a K_i value of 5.6 ± 1.0 nM exhibiting also high affinity for hNTS1 receptor ($K_i = 5.5 \pm 1.7$ nM), whereas peptide **14** was found to be the most active toward hNTS1R ($K_i = 4.2 \pm 0.62$ nM) and fewer potent at hNTS2R ($K_i = 5.8 \pm 0.65$ nM). However, both peptides showed some differences in their hNTS1R/hNTS2R selectivity: While the introduction of Cav^9 in **13** resulted in loss of selectivity (SI = 0.98), the single modification with Cav^8 in **14** led to an increase of selectivity toward the hNTS1 receptor (SI = 0.72). This result is not surprising when considering that **14** possesses one N-terminal modification with the same amino acid sequence as the parent hNTS1-selective agonist NT(8–13). The findings from the radioligand binding assays suggest that the position and number of the introduced Arg-mimicking canavanine residues in the NT(8–13) core exerts a major impact on the ionic interactions within the binding pocket of the ligands in the NTRs. In general, single modification in the N-terminus of NT(8–13) by replacement of Arg^8 or Arg^9 by a canavanine resulted in a minor loss of binding affinity (and selectivity) to hNTS1 and hNTS2R. However, these modifications led to dually active and potent compounds.

Table 1
Receptor binding data for human NTS1 and NTS2 receptor of the reference NT(8–13) (**2**) and the ligands **9**–**14**.

compd	sequence	K_i binding (nM) [a] (experiment)		$K_{i\ HYDE}$ range (nM) [b,c] (prediction)		
		hNTS1	hNTS2	hhNTS1	hhNTS2	SI [d]
2	H-Arg-Arg-Pro-Tyr-Ile-Leu-OH	0.68 ± 0.04 [e]	1.8 ± 0.17 [e]	0.13–12.6	4.28–425	0.38
		0.14 ± 0.01 [f]	1.2 ± 0.17 [f]			0.12
		1.07 ± 0.05 [g]	6.57 ± 2.18 [g]			0.16[f]
9	H-Pro-Tyr-Ile-Leu-OH	>50,000 [h]	>50,000 [h]	n.a.	n.a.	n.a.
10	H-Lys-Cav-Pro-Tyr-Ile-Leu-OH	6.9 ± 0.59	6.5 ± 0.63	0.10–10.3	3.23–321	1.06
11	H-Cav-Lys-Pro-Tyr-Ile-Leu-OH	15 ± 4.5	14 ± 4.4	0.15–15.0	0.31–30.5	1.07
12	H-Cav-Cav-Pro-Tyr-Ile-Leu-OH	60 ± 5.4	54 ± 11	0.35–34.7	3.47–344	1.11
13	H-Arg-Cav-Pro-Tyr-Ile-Leu-OH	5.5 ± 1.7	5.6 ± 1.0	2.35–233	2.94–292	0.98
14	H-Cav-Arg-Pro-Tyr-Ile-Leu-OH	4.2 ± 0.62	5.8 ± 0.65	1.19–118	1.56–154	0.72

[a] Determined by radioligand competition binding with [^{3}H]**2** at HEK293T cells; unless otherwise stated, the K_i values in nM ± SEM are the means of three (at hNTS1R), four (for hNTS2R; **2**, **10**–**13**) or five (for hNTS2R; **14**) individual experiments, each performed in triplicate.
[b] Estimated HYDE K_i range values using SeeSAR [49].
[c] $K_{i\ HYDE}$ ranges only for the selected/best docking poses from the molecular docking experiments.
[d] Selectivity index: SI = K_i (hNTS1R)/K_i (hNTS2R).
[e] K_D value in nM ± SEM.
[f] Data are from ref. 24.
[g] Data are from ref. 25.
[h] K_i value in nM from two independent experiments ($n = 2$). h = human. hh = human homolog. n.a. = not applicable.

2.5. Functional studies at hNTS1R

In order to investigate the intrinsic activities of the investigated peptides **10**–**14** and their precursor – tetrapeptide **9** in comparison to the full NTS1R agonist NT(8–13), we performed functional studies using an inositol monophosphate (IP) accumulation assay to determine the $G\alpha_q$–mediated modulation of IP production in HEK-293 cells expressing hNTS1 receptor [61]. The results are summarized as EC_{50} and E_{max} values in Table 2 and as full curves in Fig. 3 for all tested compounds.

With the exception of tetrapeptide **9**, compounds **10**–**14** displayed high activities for hNTS1R with EC_{50} values in the subnanomolar range, which are close to or even higher than the values obtained for NT(8–13). In general, the results also suggest that all tested peptides are full agonists of the hNTS1 receptor, since their E_{max} values are equal or close to the reference NT(8–13) (EC_{50} = 0.88 nM and EC_{max} = 100%) (cf. Table 2).

Regarding the impact of different modifications at positions 8 and/or 9 of NT(8–13), the most active analog within the series was found to be the single modified analog **13** (Cav^9 *vs.* Arg^9) (EC_{50} = 0.74 ± 0.19 nM; E_{max} = 96%) as well as the double substituted peptide **10** (EC_{50} = 0.82 ± 0.16 nM; E_{max} = 97%), both differ only in their modification at position 8 (Arg^8 for **13**, Lys^8 for **10**). Comparing to NT(8–13), both peptides comprise a canavanine residue instead of arginine at position 9. The EC_{50} value obtained for the single modified analog **14** (EC_{50} = 0.89 ± 0.15 nM) is equal to that of NT(8–13) (EC_{50} = 0.88 ± 0.10 nM) at E_{max} of 100% activation of hNTS1R. These results are in agreement with those observed for **14** in the radioligand binding assays, in which **14** was evaluated as the most active one at the hNTS1 receptor with a K_i value of 4.2 nM (cf. Table 1). As mentioned above, compound **14** differs from the core structure of NT(8–13) by the substitution of only one residue at the N-terminal (Cav^8 *vs.* Arg^8) comprising the same amino acid sequence as the parent peptide. Replacement of both arginine residues at positions 8 and 9 in NT(8–13) with Cav^8 and Cav^9 in peptide **12** resulted in a >1.7-fold decrease in NTS1R activation (EC_{50} = 1.30 ± 0.26 nM; E_{max} = 97%), compared to **13**. This result confirms our observation that the double modification of Arg^8 and Arg^9 by Cav in **12** is unfavorable not only for binding affinity, but also for hNTS1 receptor activation. In contrast, double or single modifications at the same positions in NT (8–13) by Lys/Cav (in **10** and **11**) or Cav (in **13** and **14**), respectively, are better tolerated in terms of binding affinity and full activation of hNTS1R. Again, reduction of the number of residues in tetrapeptide **9** resulted in a significant decrease of the effect (EC_{50} = 3200 nM). Thus, compound **9** is a weaker agonist of the hNTS1 receptor (E_{max} = 100%).

The concentration-dependent curves (log[agonist] *vs.* response) obtained for the functional tests for the activation of IP accumulation of hNTS1R in comparison to NT(8–13) are presented in Fig. 3. The curves represent the achieved activation of the receptor for compounds **9**–**14** as percentage of the NT(8–13) concentration (% accumulation of IP) required for full agonistic effect (equal to 100%). Finally, all investigated compounds appear to act as peptidomimetics of the endogenous full agonist NT.

Table 2
Functional properties for human NTS1 receptor activation of peptides **9**–**14** in comparison to the reference compound NT(8–13) (**2**).

Compd	G-protein activation [a]	
	EC_{50} (nM) [b]	E_{max} (%) [c]
2	0.88 ± 0.10	100
9	3200 ± 320 [d]	100 ± 3.0 [e]
10	0.82 ± 0.16	97 ± 1.0
11	0.85 ± 0.06	99 ± 2.0
12	1.30 ± 0.26	97 ± 2.0
13	0.74 ± 0.19	96 ± 1.0
14	0.89 ± 0.15	100 ± 2.0

[a] IP-One® assay (Ciscbio) with HEK293T cells transiently transfected with human NTS1R.
[b] EC_{50} values in nM ± SEM indicating mean potencies derived from three to nine individual experiments each done in duplicate.
[c] E_{max} values in percentage ± SEM indicating the maximum efficacy relative to the full effect of **2** (=100%).
[d] EC_{50} in nM ± SD (n = 2).
[e] E_{max} in percentage ± SD (n = 2).

2.6. Computational analysis of analog binding to hNTS1R and hNTS2R

Molecular docking studies were performed in order to investigate the binding properties and energies of all NT(8–13)-based peptides at both human NTRs. The very recently reported X-ray structure of rNTS1R (PDB ID: 6YVR) [45] bound to NT(8–13) and the cryo-EM structure of hNTS1R-G_{i1} (PDB ID: 6OS) [46] in complex with JMV449 provided valuable information about the conformational requirements and binding properties of the ligands that are crucial for activation of NTS1R. The homology models of both NTS1R and NTS2R, as their extracellular 3D architecture is almost similar (described above), as well as the 2D-NMR structures of peptides **10** and **13** were used to facilitate docking experiments. Aiming at initially predicting the binding affinity and putative binding modes of the investigated NT(8–13) analogs, the ligand binding site of the hNTS1R-G_{i1} complex in its canonical conformational state [46] was included into the homology models of hNTS1 and hNTS2 and used for further docking experiments (Figs. S7 and S8). Using SeeSAR, we next performed a structural alignment of the cryo-EM of hNTS1R (6OS9) [46] with the homology models of hNTS1R and hNTS2R. This was supposed to enable estimation of the common structural (conformational) features of their binding sites, with a focus on the extracellular part of the receptors. It turned out that the cryo-EM structure of hNTS1R showed about 90% and 53% amino acid sequence identity with the homology models of hNTS1R and hNTS2R, respectively (cf. Fig. S7). Examination and superposition of the binding pockets revealed their similar arrangement within the ECL-2 and ECL-3 of all three receptors, yet distinguishable differences in the direction of ECL1/TM2 and thus in the ligand-binding cavity between both hNTS1 receptors and the homology model of hNTS2R. However, the ligand-receptor binding sites revealed a hydrophobic (S1) and a hydrophilic subpocket (S2) within the extracellular end of the receptors (cf. Fig. S7). Additionally, the binding model of NT(8–13) was built and optimized within the binding site of hNTS1R, and used as a structural basis throughout docking experiments with SeeSAR (cf. Fig. S8).

To compute estimations of binding affinities ($K_{i\ HYDE}$ ranges), we employed the HYDE scoring function as implemented in SeeSAR [63–65]. HYDE estimates the energy of binding (Gibbs free energy ΔG, kJ/mol) summing up dehydration and hydrogen bond terms that are described by atomic increments based on experimentally determined log*P* values (cf. Experimental section) [63–65]. Coarsely approximating, HYDE enables an estimation of the thermodynamic profile of each investigated peptide within the binding pocket of the respective hNTS1 and hNTS2 receptor. Moreover, HYDE allowed us to optimize and validate the obtained conformations of each best-ranked pose with regard to torsions/bindings, as well as intra- and intermolecular clashes within the respective ligand–receptor complex.

Based on the docking protocol and the (re-)scoring procedure described in this study, we assessed the thermodynamic profiles for each investigated NT(8–13) analog within the binding site of the hNTS1 and hNTS2 receptors. Enthalpic and entropic effects of all investigated NT (8–13) analogs were computed with HYDE considering the best docking poses of each peptide in the homology models of hNTS1R and hNTS2R (Fig. S9). The obtained thermodynamic profiles of the compounds showed non-favorable entropic terms and predominantly enthalpic contributions to the total binding energy ΔG, ranking from −43.8 (**13**) to −51.2 kJ/mol (**10**) for hNTS1R, as well as between −38.2 (**2**) and −48.7 kJ/mol (**11**) for hNTS2R (cf. Fig. S9, top). This suggests a slightly preferable binding of **2** and **10**–**14** to hNTS1R than to the binding site of hNTS2R.

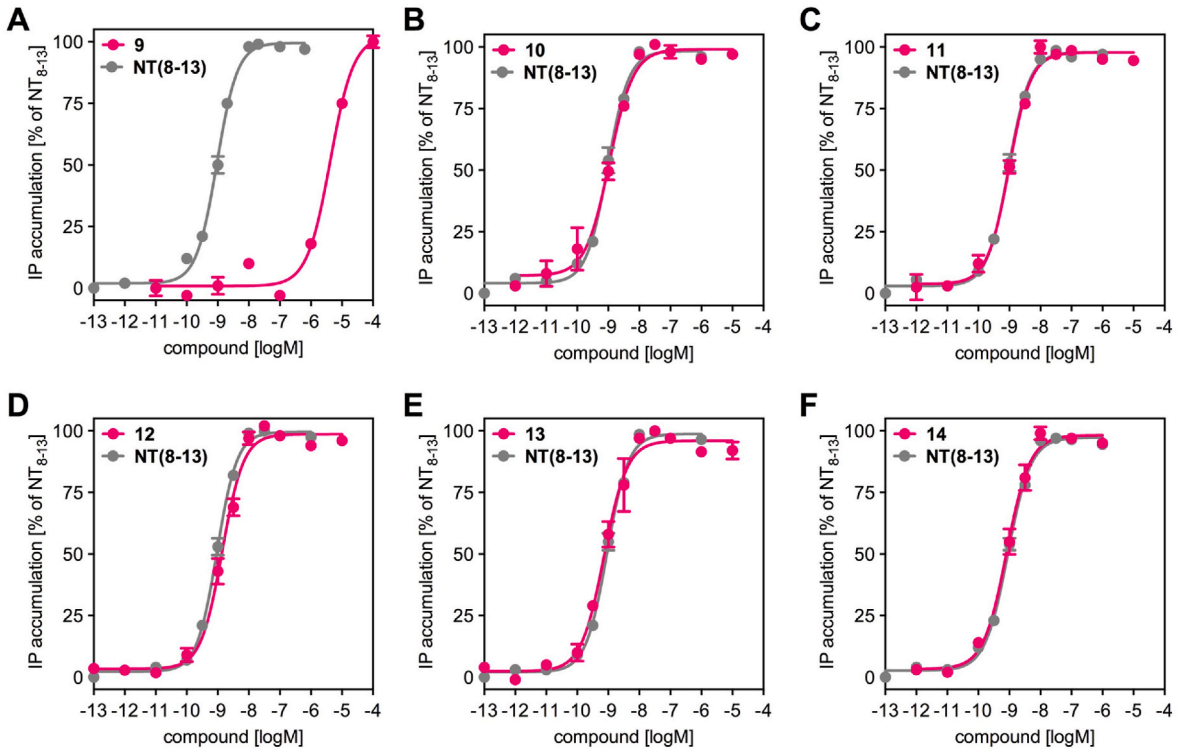

Fig. 3. Investigation of hNTS1R agonism of peptides **9**–**14** (A–F) in an IP accumulation functional assay for G-protein mediated signaling using HEK-293T cells and NT(8–13) (**2**) as a reference. Data represent mean values ± SEM from three independent experiments.

The results from the HYDE analysis suggest that the main activity of **2** and its investigated analogs toward NTRs is mainly driven by enthalpic ligand-receptor interactions (ΔH), i.e., hydrogen bonds formed between peptide and receptor residues, and not by dehydration effects (TΔS) that are related to loss/gain of lipophilic contacts within the ligand binding pocket. Importantly, the HYDE estimated binding affinities (ΔG) for all studied compounds reproduced very well their predicted $K_{i\ HYDE}$ ranges (low nM to pM). Furthermore, we found that the HYDE best-scored pose ($K_{i\ HYDE}$ ranges) for each compound (**2** and **10**–**14**) was confirmed by experiment (cf. Table 1 and Fig. S9, bottom). Some differences between predicted thermodynamic (ΔG values) and experimentally confirmed receptor binding affinities (K_i values) remain: Peptides **10** (ΔG = −51.2 kJ/mol) and **11** (ΔG = −48.7 kJ/mol), for example, were predicted to show the highest thermodynamic binding affinities at hNTS1R and hNTS2R, respectively (cf. Fig. S9, top). For comparison, their experimental K_i values were found to be 6.9 ± 0.59 nM (**10**) and 14 ± 4.5 nM (**11**), but still within the HYDE estimated ranges ($K_{i\ HYDE}$ of 0.10–10.3 nM for **10** *vs.* hNTS1R; $K_{i\ HYDE}$ of 0.31–30.5 nM for **11** *vs.* hNTS2R) (cf. Table 1).

HYDE visual assessment of binding and torsional analysis of the best ranked docking poses for **10** and **11** in the homology models of hNTS1R and hNTS2R, respectively, indicated a thermodynamical stabilization for both docking poses via formation of two intramolecular hydrogen bonds, leading to a more favorable conformation of the N-terminal residues Lys^8 and Cav^9 (**10**) and Cav^8 (**11**) (Figs. S10 and S11). Considering SeeSAR's coloring scheme of torsions [66], the best scored docking poses of **10** and **11** showed also some differences. While the torsion angles in **10** displayed a likely optimal ligand conformation within hNTS1R (most favorable "*green*" torsions), the torsional analysis for **11** suggested a less favorable ligand conformation within hNTS2R (rarely/not observed "*red*" torsions) (cf. Figs. S10 and S11). Acknowledging the fact that the torsion coloring roots in a statistical analysis, we achieved comparably trustworthy conformations (especially at positions 8 and 9) for each peptide bond and docking model (cf. Table 1 and Fig. S9).

Docking models of all investigated peptides are based on the homology structures of hNTS1R and hNTS2R to compare interactions within the obtained ligand-receptor binding modes with respect to native NT(8–13) (**2**). In general, the binding modes and estimated affinities suggest that **10**–**14** occupy the same ligand-binding cavity space within both hNTS1R and hNTS2R as determined for **2**. Moreover, the generation of poses within the binding pockets of hNTRs and re-assessing the geometries of **10**–**14** in SeeSAR resulted in similar conformations to those of **2**. Peptides **10**–**14** and **2** largely share the same binding site with both NTRs, which may be contributed to the good overlap of the common C-terminal sequence (Pro^{10}–Tyr^{11}–Ile^{12}–Leu^{13}), leading to highly similar contacts in the lower part of the binding pockets. However, as expected from their structural pattern, the binding modes of **10**–**14** and **2** revealed different conformations at the N-terminal positions 8 and 9 near the extracellular end of both receptors, leading to weaker interactions and thus to differences in binding affinity (ligand-receptor hydrogen-bond interactions at hNTS1R and hNTS2R are summarized in Tables S5–S7). From the binding modes of **2** and **10**–**14** in hNTS1R it can be seen that the C-terminal tetrapeptide sequence Pro^{10}-Tyr^{11}–Ile^{12}–Leu^{13} of the ligands occupies a binding pocket dominated by hydrophobic amino acids, forming common H-bonds with Leu^{53}, Tyr^{145}, Thr^{225} (except **10**), Arg^{212} (except **12**), Arg^{322}, and Tyr^{342} (Fig. 4 and S12). Compound **10** comprising Lys^8 and Cav^9 residues at its N-terminus appears to be involved in fewer hydrogen bonds with the hNTS1 receptor than **2** (6 *vs.* 9 H-bonds), which could account for its slightly lower receptor binding affinity (Fig. 4A and S12). However, according to the modeling the intramolecular bonds observed for the charged Lys^8 and Cav^9 residues in **10** lead to conformational changes of its N-terminal part and different binding to the extracellular subpocket of hNTS1R (Fig. 4B and C). While peptide **2** interacts via strong H-bonds with Glu^{53} and Leu^{54}, compound **10** establish H-bonds with Leu^{54} and Asp^{55} in the same orthosteric cavity of hNTS1R (cf. Fig. 4C and Table S5). A similar ligand-receptor binding situation was computed for the docking models of compounds **11**–**14** to hNTS1R. Compared to **11** and **12**, for which no intramolecular bonds were found,

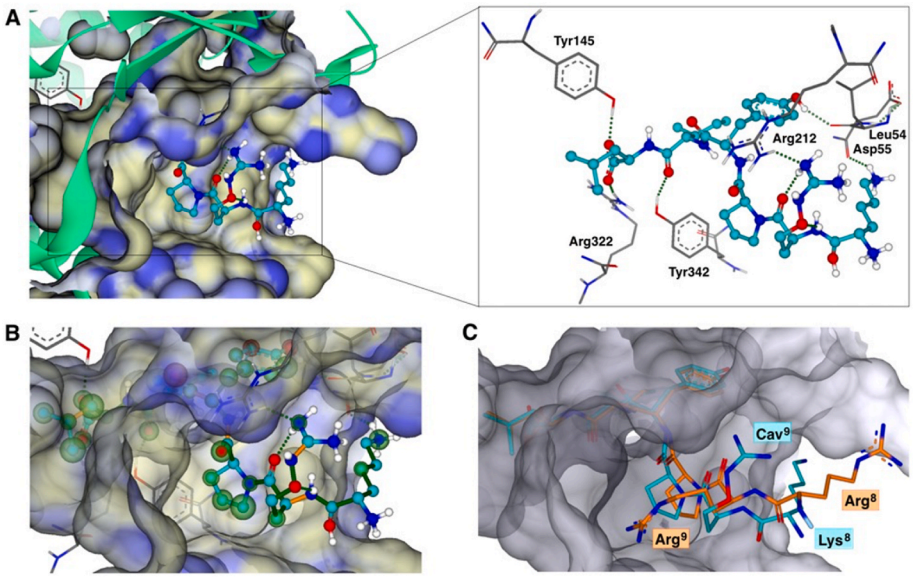

Fig. 4. Docking model of peptide **10** (cyan, A) obtained from its best-scored docking pose into the homology model of hNTS1R (green ribbons) using SeeSAR [49]. In (A), the ligand is represented as balls and sticks, and the receptor residues involved in H-bonding (dotted lines) are shown as wire-frame and labeled. The binding site of hNTS1R is colored by lipophilicity. B) Representation of HYDE and torsional analysis (as implemented in SeeSAR) for **10** within the binding site (transparent surface with lipophilicity coloring). HYDE visual affinity assessment: green = favorable, red = unfavorable and non-colored = not relevant for affinity. C) Superimposition of NT(8–13) (orange) and **10** (cyan) within the binding site of the hNTS1R (transparent grey). The residues at positions 8 and 9 for both ligands are highlighted. Note that the numbering of receptor residues is based on the homology model of hNTS1R.

the singly modified analogs **13** and **14** established one intramolecular bond while forming 11 and 8 H-bonds with hNTS1R, respectively (Figs. S12C and S12D).

The main differences in binding of **10**–**14** at hNTS1R can be seen for the amino acid residues at the N-terminal positions 8 and 9 extending the extracellular space of the receptor and thus contributing to the compound's binding affinity (Fig. 4C and S12E).

Similar observations can be made for the binding modes of **2** and **10**–**14** to hNTS2R. The C-terminal tetrapeptide sequence Pro^{10}-Tyr^{11}–Ile^{12}–Leu^{13} of the ligands occupies a binding pocket surrounded mainly by hydrophobic residues, forming common H-bonds with Ser^{93} (except **10**), Tyr^{112}, Arg^{316}, Tyr^{320}, Trp^{328} (except **12**), and Tyr^{326} (Fig. 5 and S13). However, the computed binding modes of the ligands to hNTS2R suggested that Tyr^{112}, Arg^{316}, Tyr^{320}, and Trp^{328} play an important role for binding affinities via establishing more than one strong hydrogen bond, e.g., C-terminal interactions between Leu^{13} and Tyr^{112}/Arg^{316} as well as H-bonds between Arg^9 or Cav^9 (for **2** and **14** or **13**, respectively) and Tyr^{320} at the N-terminal (Fig. 5A and S13A–D). In addition, the N-terminal residues Arg^8 (**13**) and Cav^8 (**14**) form two H-bonds with Trp^{328}, which could account for their higher binding affinity to hNTS2R compared to **11** and **12**. It seems that the multiple H-bond interactions of Leu^{13} and Arg^9 or Cav^9 could stabilize the ligand conformations within the binding cavity of hNTS2R, in addition to the higher number of intramolecular bonds (except of **10**) than in hNTS1R.

Compared to **2** and **11**–**14**, the binding mode of compound **10** shows a different orientation of Tyr^{11} and quite an extended positioning of its Cav^8 residue outside the extracellular cavity of hNTS2R, which could explain the lack of intramolecular bonds. In contrast, peptide **13** shows a similar orientation and conformation of the pentapeptide sequence Cav^9–Pro^{10}–Tyr^{11}–Ile^{12}–Leu^{13} to the one of **2**, which results in similar interaction with hNTS2R (Fig. 5).

Overall, the predicted binding modes of the investigated peptides **10**–**14** are similar to the one of the C-terminal tetrapeptide sequence of NT(8–13), yet differ in the extracellular side of both NTRs. Furthermore, the estimated binding affinity of these NT(8–13) analogs seems to be driven by H-bonds mainly with tyrosine and arginine residues.

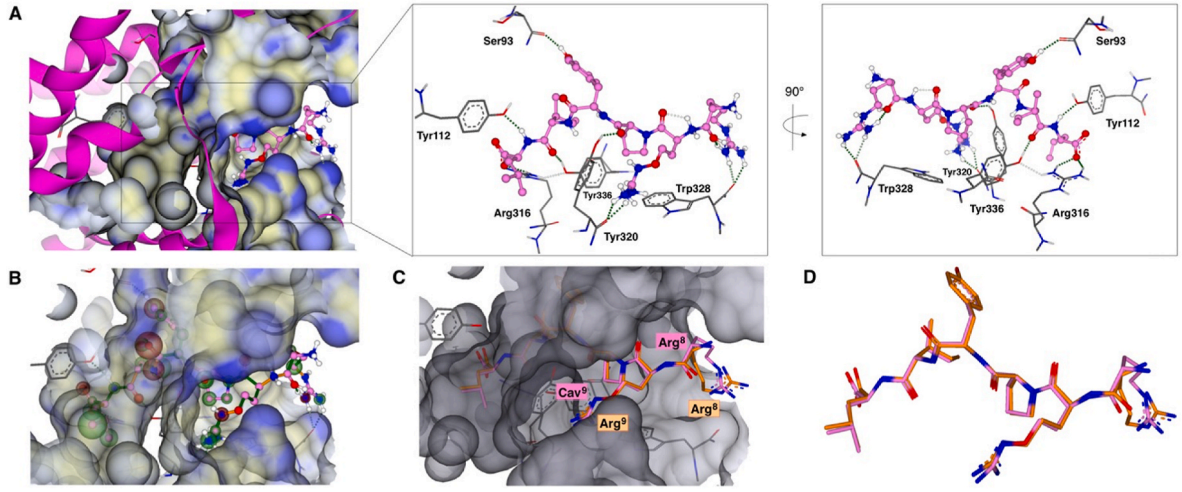

Fig. 5. Docking model of peptide **13** (magenta, A) obtained from its best docking pose into the homology model of hNTS2R (magenta ribbons) and HYDE and torsional analysis of **13** (B). The ligand and receptor representation, HYDE visual assessment and H-bonding are shown as described in Fig. 3 and computed using SeeSAR [49]. HYDE visual affinity assessment: green = favorable, red = unfavorable and non-colored = no relevant for affinity. C) Superposition of NT(8–13) (**2**) (orange) and **13** (magenta) within the binding site of the hNTS2R (transparent grey). The residues at positions 8 and 9 for both ligands are highlighted. D) Superposition of both ligands as extracted from the binding site of hNTS2R. Note that the numbering of receptor residues is based on the homology model of hNTS2R.

Additionally, intramolecular H-bonds stabilizing the conformation of the N-terminal amino acids at positions 8 and/or 9 in **10**–**14** were suggested by the modeling. Thus, we can also assume that compounds **10**–**14** are able to mimic the main interactions of NT(8–13) within the active site of both hNTS1R and hNTS2R and, thus may have similar pharmacological properties as the native peptide NT (**1**).

2.7. In vitro ADME-T studies

Evaluation of relevant physicochemical and ADME-T parameters is a key step for early-stage drug development. Poor ADME-T parameters, including stability and permeability, could be a limiting factor for preclinical investigations and a major reason to exclude a drug candidate from further clinical studies. For this purpose, relevant *in vitro* assays were performed for selected compounds **10**, **13**, and the reference **2**, while toxicity tests were carried out with all compounds of the series. The obtained results from the different *in vitro* assays are summarized in Table 3.

The cytotoxicity of all investigated compounds **2** and **9**–**14** was evaluated according to our previous protocol [67]. The effects of compounds on the viability of human hepatocarcinoma HepG2, breast adenocarcinoma MDA-MB-231, and colon adenocarcinoma HT-29 cells were determined after a 24 h incubation period in a concentration range of 0.1–100 μM. The cytotoxicity profile for the representative compounds **10** and **13** followed the same trend in all three cell lines as observed for the control (untreated groups) at all tested concentrations and thus no pronounced effect on cellular viability was detected (Fig. S14, Table 3). Similarly, none of the other tested compounds (**2**, **9**, **11**, **12**, and **14**) showed any cytotoxic effect after 24 h incubation with the same human cell lines and at the same concentration range (0.1–100 μM) (Fig. S15).

Next, we investigated compounds **10**, and **13** for their ability for drug-drug interactions using CYP inhibition assays. Notably, the tested compounds did not inhibit the most important CYP1A2, CYP3A4, CYP2B6, CYP2C9, and CYP2D6 enzymes at the highest tested concentration of 50 μM (cf. Table 3).

Table 3
In vitro ADME-Tox and physicochemical parameters of NT(8–13) (**2**), **10** and **13**.

	10	13	2
Cytotoxicity assay (% of control ± SD @100 μM)			
HepG2 viability	95.1 ± 4.4	99.8 ± 4.0	96.0 ± 0.6
MDA-MB-231 viability	97.3 ± 0.7	97.7 ± 1.5	93.3 ± 6.7
HT-29 viability	94.6 ± 1.3	88.9 ± 2.4	90.7 ± 1.8
CYP inhibition (@50 μM)			
CYP2B6	No inhibition	No inhibition	No inhibition [a]
CYP1A2	No inhibition	No inhibition	No inhibition [a]
CYP2C9	No inhibition	No inhibition	No inhibition [a]
CYP2D6	No inhibition	No inhibition	No inhibition [a]
CYP3A4	No inhibition	No inhibition	No inhibition [a]
Aqueous solubility (mg/mL, @pH 7.4)	>100	>100	n.d./> 100 [a]
LogD$_{7.4}$	<0	<0	n.d./< 0 [a]
LogP [a]	−0.70	−1.56	−1.10
Peptide stability (@50 μM)			
% remaining @24 h, pH 2.0/pH 7.4	100/100	100/100	100/100
% remaining after 30 days, pH 2.0/pH 7.4	>97/> 100	>94/> 95	>97/100
PAMPA-BBB permeability			
P_e (× 10^{-6} cm/s), donor pH 7.4/acceptor pH 7.4	2.81 ± 0.45	0.89 ± 0.10	0.64 ± 0.20
–logP_e	5.55 ± 0.07	6.05 ± 0.03	6.21 ± 0.13

[a] Predicted values at the neutral state of the respective peptide using SeeSAR software tool.[50] n.d. = not determined.

To access the most important physicochemical properties of the investigated NT(8–13) analogs, we determined the aqueous solubility and the distribution coefficient (Log*D*, *n*-octanol-buffer 20 mM at room temperature) of compounds **10** and **13** at physiologically relevant pH 7.4. Lipophilicity (expressed as Log*P*), which is as a key parameter affecting several other physicochemical and biological properties of drugs, was additionally calculated for **2**, **10** and **13** using SeeSAR. As expected, peptides **2**, **10** and **13** showed excellent aqueous solubility (>100 mg/mL at pH 7.4) combined with low lipophilicity values (Log$D_{7.4}$ < 0) (cf. Table 3).

The chemical stability of **2**, **10** and **13** was investigated in PBS (50 μM sample concentrations) under physiologically relevant pH 2.0 and 7.4 (pH-dependent) at room temperature and 37 °C over a period of 30 days (time-dependent). For this purpose, we performed short-term studies by measurement of peptide stability (at 37 °C) in the interval 0–24 h using UV/Vis spectroscopy (Fig. S16). For performing long-term studies, the same samples from the UV/Vis measurements were stored for 30 days under daylight exposure and subsequently analyzed by RP-HPLC. Under these conditions, the studied peptides **2**, **10**, and **13** appeared to be stable for long-time use (Fig. S17 and Table 3).

In addition to the physicochemical and ADME-T properties, the blood-brain barrier (BBB) permeability of **2**, **10**, and **13** was determined using a parallel artificial membrane permeability assay (PAMPA). In general, PAMPA-BBB is widely used for transcellular permeability assessment of a drug's ability to penetrate into the brain by passive diffusion and, thus, to predict possible *in vivo* BBB permeability [67–71]. The BBB permeability of **2**, **10**, and **13** was measured in PBS (100 μM) at pH 7.4 after 4 h incubation at room temperature (cf. Table S8, Figs. S18 and S19). PAMPA results showed that the Lys^8/Cav^9-modified analog **10** exhibits satisfactory ability to cross BBB by passive diffusion with an effective permeability (P_e) value higher than the required limit for permeable compounds ($P_e \geq 1.5 \times 10^{-6}$ cm/s).[71] Moreover, compound **10** exhibited considerably higher BBB permeability ($P_e = 2.81 \times 10^{-6}$ cm/s) than the standard drug theophylline (low permeable) and the parent peptide NT(8–13) ($P_e = 0.64 \times 10^{-6}$ cm/s). In contrast, Cav^9-modified analog **13** showed indeed higher permeability than **2** and theophylline, but it can be classified as low BBB permeable (Fig. S19, Table 3).

According to our results from the ADME-T studies and evaluation of key physicochemical parameters, compounds **10** and **13** can be classified as highly stable with well-balanced solubility-lipophilicity properties and excellent safety profile as estimated for the native peptide NT (8–13) (**2**), too. With regard to PAMPA-BBB permeability, compound **10** can be highlighted because of its increased ability (>4-fold compared to **2**) to cross the BB barrier and thus enter the brain by transcellular passive diffusion. However, it should be considered that in addition to the passive diffusion, which is typical for small CNS drugs, peptides can also penetrate into the brain by active influx transport [71]. Therefore, compound **10** was considered for further *in vivo* studies.

2.8. Behavioral effects

Based on its high NT receptors affinity and potent functional activity combined with high stability and improved BBB permeability, compound **10** emerged as a suitable candidate for further *in vivo* pharmacological evaluation. NT and its NT(8–13) analogs are known for their potent neuromodulatory and neuroprotective effects, including stimulation of DA release [7,18,72], demonstrated in rat models of PD as well [1,19,20]. In this study, the behavioral effects of compound **10** were compared to those of NT(8–13) (**2**), the parent compound with the highest binding affinity and NTS1/NTS2 selectivity.

The behavioral effects of **10** and **2** were tested in a mouse model of MPTP (1-methyl-4-phenyl-1,2,3,6-tetrahydropyridine)-induced PD, evaluating their ability to restore memory and motor functions in male

BALB/c albino mice after neurointoxication with MPTP (Fig. 6). Following an adapted procedure [73], the animals in the different groups were treated intraperitoneally (i.p.) for five consecutive days with either MPTP, a combination of compound **2** and MPTP or a combination of compound **10** and MPTP, with MPTP being injected 1 h after application of the respective compound (**2** or **10**). In the case of the control group, the animals were injected with saline (Fig. 6A). The behavioral tests were carried out 10 days after the first MPTP treatment (cf. Fig. 6A) and the body weights of animals were measured on the 1st, 5th, and 10th day of the experimental procedure (Fig. 6B).

As indicated, compared to the initial body weight of all groups, animals in the MPTP, positive control, and test group (treated with compound **10**) showed minor weight loss five days after treatment, while those in the control group did not show any. Interestingly, the animals in the MPTP and the test group pretty much recovered their body weight ten days after treatment, while an increase in the body weight was observed for the animals in the positive control group (treated with compound **2**).

The behavioral effects of **10** and **2** were first tested in a step-through passive avoidance test [74,75], measuring their ability to increase the step-through latency (STL), decreased by MPTP applications, thus restoring memory performances in mice with MPTP-induced PD (Fig. 6C). As the figure shows, ten days after the first MPTP treatment the STL values in the MPTP group were significantly decreased (by more than 60%, $p < 0.001$) as compared to the control group. In both the positive control group (MPTP + **2**) and the test group (MPTP + **10**) those values increased, compared to the MPTP-treated group, and control values restored (no significant differences were observed between the control group and the MPTP + **2** group as well as between the control group and the MPTP + **10** group), showing the favorable effects on memory of both compounds **2** and **10**.

Next, using the hanging test, the two compounds were also examined for their effects on the motor function of MPTP-treated mice (Fig. 6D). Several motor functions including balance, coordination and muscle strength were evaluated [76–79]. Fig. 6D shows that ten days after the first MPTP treatment, the hanging time values in the MPTP group were significantly decreased (by 54%, $p < 0.01$) as compared to the control group. In both the positive control group (MPTP + **2**) and the test group (MPTP + **10**) those values increased compared to the MPTP-treated group, but the increase induced by the application of compound **10** was much larger than that, induced by compound **2** and reached statistical significance (MPTP *vs.* MPTP + **2**, 31% increase, $p > 0.05$ and MPTP *vs.* MPTP + **10**, 87% increase, $p < 0.05$), indicating the bigger efficacy of compound **10** in restoring motor functions of PD-mice.

Since the behavioral tests revealed that compound **10** (10 mg/kg, i.p.) significantly improved memory and motor skills (function) in MPTP-treated mice, we further investigated whether **10** prevents the loss of dopaminergic neurons induced by neurotoxicity and compared the results with those for the reference compound **2**. For this purpose, we evaluated the effects of **2** and **10** on the attenuation of the MPTP-induced nigrostriatal dopaminergic neuronal damage by counting the number of TH-immunoreactive (positive) cells in substantia nigra (SN)

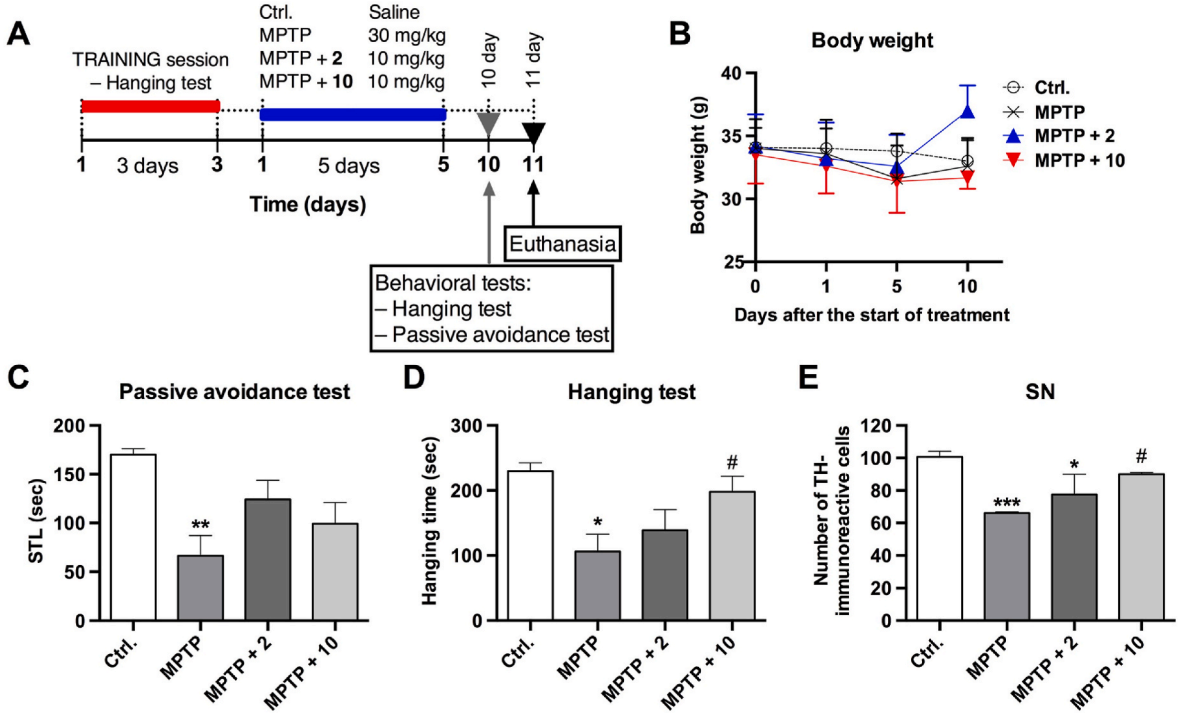

Fig. 6. *In vivo* effects of the reference neuropeptide NT(8–13) (**2**) and compound **10** in a mouse model of MPTP-induced Parkinson's disease. (A) Experimental design of the *in vivo* studies. Before the start of injections, the mice were trained for three consecutive days for the hanging test. The animals were divided into four groups ($n = 5$ animals/group) and injected intraperitonially (i.p.), once a day for five consecutive days, with either saline (control group), MPTP (30 mg/kg), MPTP + **2** (10 mg/kg), or MPTP + **10** (10 mg/kg). In the test groups, where the reference NT(8–13) (**2**) (positive control) or peptide **10** were applied, MPTP was injected 1 h after the injection of the respective compound. The behavioral tests and further euthanasia were carried out on the 10th and 11th day after the start of MPTP (saline) injection, respectively. (B) Body weight change in mice with MPTP-induced PD after treatment with MPTP, MPTP + compound **2** and MPTP + compound **10** in comparison with the control group treated only with saline. (C) Effects of compounds **2** and **10** on the memory disturbances in an MPTP-induced PD model in mice assessed by the step-through passive avoidance test. (D) Effects of compounds **2** and **10** on the motor disturbances in an MPTP-induced PD model in mice evaluated by the hanging test. (E) Attenuation of the MPTP-induced nigrostriatal dopaminergic neuronal damage in substantia nigra (SN) by **2** and **10**. SN was evaluated eleven days after the start of MPTP-intoxication/peptide injection. Quantification was carried out by counting the SN TH-immunoreactive cells. Values are expressed as mean ± SEM in percent with the number of positive TH-cells in the control group taken as 100%. Statistical analysis for all tests was performed by one-way ANOVA followed by Dunnett's multiple comparison test: *, $p < 0.05$; **, $p < 0.01$; ***$p < 0.001$ as compared to the saline-injected group; #, $p < 0.01$ as compared to the MPTP-injected group.

(Fig. 6E). The day after the animals were subjected to the behavioral tests, SN samples were obtained and subsequently stained with a tyrosine hydrolase (TH) antibody and quantified (cf. Experimental section) [72,74,78].

Our results showed that mice treated with MPTP exhibited a lower number of TH-positive neurons compared to the control group (66 ± 1.41% for the MPTP-treated group *vs.* 100.7 ± 6.02% for the control group, $p < 0.001$); large cell-depleted areas and extracellular depositions were observed as well. Compound **2** did not manage to alleviate the MPTP-induced damage and a statistically significant difference was observed in the number of TH-positive neurons between the control and the MPTP + **2** group (100.7 ± 6.02% for the control group *vs.* 77.5 ± 6.25% for the MPTP + **2** group, $p < 0.05$). On the other hand, compound **10** greatly relieved MPTP-induced neurotoxicity as no significant difference was observed between the control and the MPTP + **10** group (100.7 ± 6.02% for the control group *vs.* 90 ± 4.0% MPTP + **10** group, $p > 0.05$), but such a difference existed with the MPTP group (66 ± 1.41% for the MPTP-treated group *vs.* 90 ± 4.0% for the MPTP + **10** group, $p < 0.05$). The above observations further identified compound **10** as a more efficient neuroprotectant compared to the parent peptide NT(8–13) (compound **2**).

3. Conclusion

In the current study, we modeled and synthesized a set of NT(8–13)-based analogs in order to evaluate their chemical and pharmacological properties associated with hNTS1 and hNTS2 receptor binding affinities. In fact, both receptor subtypes represent promising targets for the development of novel NT analogs for the treatment of PD. Consequently, we designed a series of NT(8–13) analogs with modifications at positions 8 and/or 9 in NT(8–13) using a molecular modeling approach to predict their binding affinity ($K_{i\ HYDE}$ range) obtained from the respective best-scored docking models within the homology models of human NTS1 and NTS2 receptors. The predicted binding modes of the investigated peptides **10**–**14** were found to be similar to that of the C-terminal tetrapeptide sequence of NT(8–13) and, thus, to mimic the main interactions of NT(8–13) within the active sites of both hNTS1R and hNTS2R (e.g., H-bond interactions mainly with tyrosine and arginine residues). Moreover, the experimental binding affinities (K_i values) for all studied compounds reproduced very well their predicted $K_{i\ HYDE}$ ranges. The importance of the residues at positions 8 and/or 9 of **2** and **10**–**14** for hNTS1 and hNTS2 receptors affinity was experimentally confirmed by radioligand binding assays. Indeed, replacement of Arg^8 and/or Arg^9 by Lys and/or Cav residues led to NT(8–13) analogs with equipotent affinity at both hNTS1 and hNTS2 receptors. Additionally, functional studies were performed using an inositol monophosphate (IP) accumulation assay to determine the $G\alpha_q$–mediated modulation of intracellular IP production, showing that all investigated compounds are full agonists of the hNTS1 receptor. Compound **10** can be highlighted due to its high binding affinity towards NTS1R and NTS2R, acting as a potent full agonist of hNTS1R. Further *in vitro* ADME-T profiling and *in vivo* behavioral studies revealed that compound **10** exhibits improved stability, safety, and BBB permeability, combined with a significant enhancement of motor and memory functions in a mouse model of MPTP-induced PD compared to NT(8–13). Our results further suggest that the herein developed dual NTS1/NTS2-active analogs represent an attractive strategic starting point for the treatment of PD and possibly other CNS disorders.

However, there are some limitations regarding the long-term stability (e.g., protein plasma stability) and, thus *in vivo* application of such NT-analogs. Thus, as the next step we will focus on the investigation of the effects of compound **10** and recently designed NT-analogs with improved stability in more advanced PD models, analgesic properties in pain-related models, as well as other *in vivo* models of Alzheimer's disease or Schizophrenia representing other neuromodulatory systems and mechanisms. In summary, we expect that the results presented herein and the envisaged future studies will reveal the therapeutic potential of NT(8–13)-based peptides.

4. Experimental section

4.1. Materials

If not otherwise stated, all solvents, reagents, and buffer chemicals were of analytical grade obtained from commercial suppliers. Further details about the chemicals are given in the Supporting information.

4.2. Synthesis of peptides and purification

4.2.1. General procedure for SPPS

Synthesis of the precursor tetrapeptide H-PYIL-OH (**9**) and the native NT-fragment NT(8–13) (**2**) was performed by automated solid-phase peptide synthesis (SPPS) based on a standard Fmoc (*N*-(9-fluorenyl) methoxy-carbonyl) protocol using a ResPep SL peptide synthesizer (Intavis Bioanalytical Instruments AG, Cologne, Germany) as described earlier [50,51]. A Leu-preloaded chlorotrityl chloride resin (0.86 mmol/g) was utilized. HBTU served as a coupling reagent and *N*-methylmorpholine was applied as a base. Prolongation of the precursor to prepare peptides **10**–**14** was performed by manual SPPS. Coupling reactions were performed in the presence of 4.0 equiv. of Fmoc-amino acid (Fmoc-Lys(Boc)-OH and Fmoc-Arg(Pbf)-OH) or 2.0 equiv. of Fmoc-Cav(Boc)-OH, 4.0 equiv. HBTU and HOBt (or 2.0 equiv. for Fmoc-Cav(Boc)-OH coupling), and 8.0 equiv. DIEA (or 4.0 equiv. for Fmoc-Cav(Boc)-OH coupling) in DMF for 90 min under ambient temperature. Subsequent Fmoc-cleavage was achieved by addition of 20% piperidine in DMF. Peptide cleavage and side-chain Boc-deprotection were accomplished with 1.0 mL/100 mg resin reagent K (75 mg phenol, 25 μL 1,2-ethandithiol, 50 μL thioanisol, 50 μL water in 1.0 mL TFA) under stirring for 3 h at room temperature. The cleavage mixture was filtered and precipitated in ice-cold diethyl ether. Peptide pellets were washed for three times with diethyl ether and re-dissolved in 80% *tert*-butanol for freeze-drying.

4.2.2. General procedure for purification of peptides

Purification of crude peptides was performed by semi-preparative RP-HPLC using a Knauer Eurospher 100 column (C18, 250 × 32 mm, 5.0 μm particle size, 100 Å pore size) on a Shimdazu LC-8A system (Duisburg, Germany) or a JASCO PV-987 instrument (Gross-Umstadt, Germany). A gradient elution system was applied with a continuous increase of eluent B (acetonitrile/water 90/10, 0.1% TFA) in eluent A (0.1% TFA in water) over 120 min at a flow rate of 10 mL/min. Detection was performed at 220 nm. Collected fractions were combined, evaporated from acetonitrile, freeze-dried, and stored at −20 °C. Peptide purity was confirmed by analytical HPLC on a Shimadzu LC-20AD system equipped with a Vydac 218 TP column (C18, 250 × 4.6 mm, 5.0 μm particle size, 300 Å pore size). Gradient elution was carried out using a gradient of 15–45% acetonitrile containing 0.1% TFA (eluent B) in 30 min and 0.1% TFA in water (eluent A) at a flow rate of 1.0 mL/min. The detection of the peptides was at $\lambda = 220$ nm. All peptides were obtained in purities >95%. Peptide yields after synthesis and purification ranged between 31 and 100% (for details, see Table S1).

4.2.3. Peptides analytical characterization

For peptides characterization the following methods were applied: analytical HPLC (see above), mass spectrometry, and thin layer chromatography (TLC). Peptide molar masses were verified by matrix-assisted laser desorption-ionization/time-of-flight (MALDI-TOF) and electrospray ionization (ESI) mass spectrometry. MALDI spectra were recorded on an ultrafleXtreme instrument, equipped with an autoflex III smartbeam, and an autoflex II laser (Bruker Daltonics, Bremen, Germany); ESI mass spectra were measured on a micrOTOF-Q III instrument (Bruker Daltonics, Bremen, Germany) [80].

4.2.4. NMR experiments

NMR spectra were recorded at 293 K in 25 mM PBS buffer pH 7.0 (92% H_2O/8% D_2O) on a Bruker Avance III HD Ascend 700 MHz cryo spectrometer with a He-CP 700 QCI H–P/C/N cryo probe. The peptides were measured at a concentration of 1.5 mM, and the backbone as well as the side chain atoms were assigned via a combination of 2D [^{1}H,^{1}H]-DQF-COSY, [^{1}H,^{1}H]-TOCSY and [^{1}H,^{1}H]-NOESY spectra using water suppression. The spectra were processed with TOP SPIN 4.0.6 (Bruker) and analyzed using CcpNmr Analysis (Collaborative Computing Project for NMR). Distance and dihedral constraints were extracted from [^{1}H,^{1}H]-NOESY spectra and the Upper-limit-distance constraints were calibrated according to their intensities in the NOESY spectra. To calculate the peptide structures based on the chemical shift data the nmr_solve macro with default parameters in YASARA version 20.4.242 was used [52]. Details of NMR experimental data for peptides **10** and **13** are presented in Tables S2 and S3, together with the 3D-coordinates of both structures that are given as PDB files (see Supporting Information).

4.3. Molecular modeling

4.3.1. Peptide-receptor docking

Unless otherwise mentioned, all computations were carried out using the SeeSAR software package [49] by applying the integrated binding site computation and docking modules. The homology models of human NTS1 and NTS2 receptor were used as input PDB structures for molecular docking studies, pose generation of target peptides, visual inspection, scoring, and re-scoring assessment of the representative ligand's best-docked poses. The respective conformations of NTS1 and NTS2 receptor binding sites were generated using the cryo-EM structure of human NTS1R in complex with the heterotrimeric G_{i1} protein (PDB ID: 6OS9, res. 3.00 Å) as a PDB input template [46]. The chain R (that comprises the binding site of the cryo-EM structure) was extracted from the heterotrimeric G_{i1} protein and further used for processing in SeeSAR (cf. Figs. S7 and S8). Water molecules were then added to the target homology models of hNTS1R and hNTS2R to complete the respective model during computational (scoring and re-scoring) steps. The 3D-structure of each peptide was then systematically built using SeeSAR's Molecule Editor mode and processed by applying the SeeSAR-integrated docking engine. A maximum of 10 poses was generated for each peptide and receptor to perform post-processing with the HYdrogen DEssolvation (HYDE) algorithm, as implemented in SeeSAR. Additionally, the applicability of the docking step was validated by unconstrained docking of all 20 poses (obtained from the 3D-NMR analyses) of peptides **10** and **13**, each of these poses used as a PDB input structure in SeeSAR docking module. The docking implemented in SeeSAR embeds the FlexX/-SIS algorithms as previously described [67,69]. Computational experiments in SeeSAR yield docking poses as a function of the empirical docking score, and, after a respective post-optimization, also in terms of the desolvation-aware HYDE computation, see below [67,69]. After visual inspection, the best-ranked docking poses of the peptides were selected and further computed in the next optimization steps within the binding sites of the homology models of hNTS1R and hNTS2R. To increase scoring stability of the complex energy landscape, a successive semi-manual conformational optimization in terms of (i) torsions/bindings, (ii) intra- and (iii) intermolecular clashes using the molecule editor module in SeeSAR was performed. The obtained optimized conformations were then re-docked and re-scored. This reflects a probing of nearby energetic states as starting points for optimizations, avoiding that one relies too much on single starting points for HYDE free energy approximations. Finally, the representative best-scored poses (conformations) of each docked peptide and for each receptor were saved in SD format and CSV data files before usage for further steps in this work (see hNTS1R and hNTS2R best poses CSV files, Supporting Information).

4.3.2. HYDE scoring and visualization

HYDE is a scoring function that is integrated in SeeSAR to rapidly compute estimations of binding affinities (ΔG) [63]. HYDE is based on the description of hydrogen bonds/salt bridges on the one hand side, and dehydration terms on the other [65–67]. In its 3D user interface, SeeSAR visualizes the (HYDE-) estimated free energy of binding affinity (ΔG) using translucent spheres (HYDE "coronas") ranging from large dark red (very unfavorable) to large dark green coloring (very favorable for affinity).[66] Corona sizes correlate with the amount of contribution of each non-hydrogen atom within the obtained/docked framework [65]. As a result, HYDE calculates the estimated binding affinity (represented in this work as $K_{i\ HYDE}$ ranges) and an approximate, respective lipophilic ligand efficiency (LLE_{HYDE}).

4.3.3. Visual inspection of torsions

The docking results were visually inspected using the assessment of the statistical significance of torsion patterns in SeeSAR [63,64,66]. It should be pointed out that the respective coloring (*red* = rarely/not observed torsions; *orange* = observed sometimes; *green* = observed often torsions) is based on statistics of occurrence of a substructure dihedral in the Cambridge Structural Database (CSD) [63,64].

4.4. Radioligand binding studies

Binding affinities towards the human neurotensin receptor subtypes NTS1 and NTS2 were determined as described previously [60,61]. The protein concentration was established using the method of Lowry [81]. The resulting competition curves were analyzed by nonlinear regression using GraphPad Prism 8.0 (San Diego, CA) to provide the respective IC_{50} values, which were subsequently transformed into the K_i values employing the equation of Cheng and Prusoff [82].

4.5. Cytotoxicity assay

4.5.1. Preparation of cell cultures

Human hepatocellular carcinoma (HepG2), human breast adenocarcinoma (MDA-MB-231), and human colon adenocarcinoma (HT-29) cells were cultured in Dulbecco's modified Eagle's medium (DMEM, Gibco, Austria) supplemented with 10% fetal bovine serum (FBS; Gibco, Austria), penicillin (100 U/mL) and streptomycin (0.1 mg/mL) solution (Gibco, USA). All cells were cultured under a humidified CO_2 (5.0%) atmosphere at 37 °C and passaged by trypsinization when reached approximately 80% confluence. For experiments, cells in exponential phase of growth (at a density of 5000 cells/well) were seeded into 96-well flat-bottom plates after treatment with trypsin-EDTA (Greiner, Germany) solution at a final volume of 100 μL/well. Cells were incubated overnight before treatment with test substances.

4.5.2. Cell viability assay

The cytotoxicity of peptides NT(8–13) (**2**), **9**–**14** (1.0 mM stock solutions in $PBS_{7.4}$) was evaluated in HepG2, MDA-MB-231, and HT-29 cell lines by colorimetric assay using 3-(4,5-dimethylthiazol-2-yl)-2,5-diphenyltetrazolium bromide (MTT) as previously reported [67].

4.6. In vivo behavioral assays

4.6.1. Animals, hosting, and habituation

Experiments were performed with 8- to 10-weeks old male BALB/c albino mice (30–35 g weight) (Erboj Laboratories, Institute of Neurobiology, BAS, Sofia, Bulgaria). Animals were kept in plastic cages (n = 3) in a quiet room under constant conditions (25 ± 3 °C, 12 h light/dark cycle) with food and water ad libitum and habituated for five days before the start of the experiment. All the experiments with mice were carried out in agreement with the institutional guidelines (Bioethics Committee at the Institute of Neurobiology, Bulgarian Academy of Sciences) in compliance with the national and international laws and

policies laws (the new Directive 2010/63/EU, September 22, 2010) of the European Parliament and the Council of the European Union (revising the older European Directive 86/609/EEC) on the protection of animals used for scientific purposes; the National Institute of Health (NIH, USA) Guide for the Care and Use of Laboratory animals (NIH Publication No. 85–23, 1985), and Bulgarian laws [75].

4.6.2. Administration and experimental design

Mice were divided into four groups (n = 5/group) and injected intraperitoneally (i.p.) as follows: a control group (Ctrl.) treated with normal saline (100 μL/10 g), a MPTP group treated with MPTP (30 mg/kg) for five consecutive days, a positive control group (MPTP + **2**) treated simultaneously with compound **2** (NT(8–13), 10 mg/kg) and MPTP (60 min after the peptide application, 30 mg/kg) for five consecutive days, and a test group (MPTP + **10**) treated simultaneously with peptide **10** (10 mg/kg) and MPTP (60 min after the peptide application, 30 mg/kg) for five consecutive days.

4.6.3. Neurobehavioral evaluation

In order to evaluate memory and motor disturbances in MPTP-induced PD in mice, a Step-through passive avoidance test (memory) and a Hanging test (motor disturbance) were performed. Three to four days before starting the experiment, the mice from all groups were trained and the tests were performed at the end of each experiment.

4.6.4. Step-through passive avoidance test

The step-through passive avoidance test was carried out as previously described [74,75]. Training and test sessions were conducted in an apparatus consisting of a dark and light compartment (chamber). The floor of the dark chamber was composed of steel rods, connected to a stimulator for delivering electro shocks. In the training session, conducted before the start of substance applications, the mouse was placed in the light compartment with its back facing the dark compartment. After opening the door, separating the two compartments and upon the mouse's entrance to the dark compartment, the door was closed, and an electric shock delivered (0.8 mA, 3 s once). The time (in sec) it took the mouse to enter the dark compartment was recorded as initial latency (IL). At the 10th day after the first injection, the mouse was placed in the light compartment for the test session, and the latency to enter the dark compartment (with a cut-off time of 180 s) was recorded as a step-through latency (STL).

4.6.5. Hanging test

The experiment was performed in two sessions, a training and a test session, as described in the literature [76–78]. In the training session, conducted for three consecutive days, preceding the treatment, mice were placed on a horizontal wire (55 cm long, diameter 2.0 mm, 37 cm above the ground) and allowed to stay on the wire until they lose control and fall. Every mouse was given the possibility for three successive attempts on each of the training days. The test session was accomplished ten days after the first treatment. Every mouse was tested in three consecutive trials, the hanging time (in sec) recorded and averaged [75].

4.6.6. Immunohistological evaluation

On the day after the behavioral tests, the brains (n = 5/group) for histological evaluation were prepared as described [76,79]. The brain samples were immersed and fixed overnight at 4 °C in 10% paraformaldehyde buffered at pH 7.4 with 0.1 M phosphate buffer. Cross sections were cut at the hippocampal area for each mouse brain and placed in biopsy cassettes for further processing in Donatello Fast automatic tissue processor (Diapath S.p.A., Martinengo, Italy). The brain samples underwent dehydration (with ethanol) and tissue cleaning (with water), and were next incorporated in paraffin. From each paraffin block, slices of 3–4 μm in thickness were prepared, selected according to the Atlas of the Mouse Brain [83] to pass through substantia nigra (SN). Samples for immunochemistry were prepared by incorporating the paraffin slices into pre-coated slides with further incubation for 1 h at 60 °C. Prior to immunohistological staining for tyrosine hydroxylase (TH), the paraffin slides were deparaffinised and rehydrated in a PT Link pre-treatment module (Dako Agilent, Santa Clara, CA, USA), following a standard protocol. Briefly, the slides were immersed into the pre-heated to 65 °C solution, containing xylol and ethanol, and incubated for 20 min at 97 °C. After cooling to 65 °C, the slides were washed twice with a washing buffer (0.01 M PBS) and pre-incubated for 5 min with 1.0% glycine at room temperature. Then, the paraffin slides (n = 5/group) were stained with rabbit anti-tyrosine hydroxylase (TH) antibody (1:500; Millipore, Bendford, MA, USA) in a Dako Autostainer Link 48 instrument (Dako Agilent, Santa Clara, CA, USA) using a standard protocol. Finally, photomicrographs were taken using a C5050Z digital system (Olympus Optical Co. ltd., Tokyo, Japan) and analyzed by counting the number of positive cells at × 20 magnification. The average number of TH-positive cells in representative SN sections was used for quantification of TH.

4.7. Statistical analysis

Data are expressed as mean ± standard errors of the mean (SEM). All graphs and the statistical analysis were performed using GraphPad Prism 6.0 (GraphPad Software, La Jolla, CA, USA). The STL (in sec) for the step-through passive avoidance test, the hanging time (in sec) for the hanging test, and the number of TH-positive immunoreactive cells were analyzed using one-way ANOVA followed by a Dunnett's multiple comparison test to compare the drug (MPTP + **2**, and MPTP + **10**) with saline- (control) and MPTP-treated groups. A difference between the groups was considered significant at p-values (* $p < 0.05$, ** $p < 0.01$ and *** $p < 0.001$ *vs.* saline; #$p < 0.01$ *vs.* MPTP group).

Funding sources

This work was funded by the Bulgarian National Science Fund (BNSF) under research grant KP-06-N59/2 (КП-06-Н59/2).

Notes

The authors declare no competing financial interest.

Declaration of competing interest

The authors declare that they have no known competing financial interests or personal relationships that could have appeared to influence the work reported in this paper.

Data availability

Data will be made available on request.

Acknowledgments

The authors thank Thomas Schmitz and Benjamin F. Schmalohr for technical assistance. Financial support by the Bulgarian National Science Fund (BNSF, contract number KP-06-N59/2, to N.T.) and the University of Bonn (to D.I.) is gratefully acknowledged. Provision of trifluoroacetic acid by Solvay GmbH (Hannover, Germany) is kindly acknowledged.

Appendix A. Supplementary data

Supplementary data to this article can be found online at https://doi.org/10.1016/j.ejmech.2023.115386.

References

[1] M.R. Iyer, G. Kunos, Therapeutic potential targeting the neurotensin receptors, Expert Opin. Ther. Pat. 31 (2021) 361–386.

[2] A.W.K. Yeung, M.G. Georgieva, K. Kirilov, A.A. Balacheva, M.I. Peeva, J. O. Horbańczuk, M. Lucarini, A. Durazzo, A. Santini, E.B. Souto, T.I. Pajapanova, L. Millela, A.G. Atanasov, N.T. Tzevtkov, Neurotensins and their therapeutic potential: research field study, Future Med. Chem. 12 (2020) 1779–1803.

[3] H.L. Woodworth, P.A. Perez-Bonilla, B.G. Beekly, T.J. Lewis, G.M. Leinninger, Identification of neurotensin receptor expressing cells in the ventral tegmental area across the lifespan, eNeuro 5 (2018) e0191–e01917.

[4] J.-P. Vincent, J. Mazella, P. Kitabgi, Neurotensin and neurotensin receptors, Trends Pharmacol. Sci. 20 (1999) 302–309.

[5] Z. Wu, D. Martinez-Fong, J. Trédaniel, P. Forgez, Neurotensin and its high affinity receptor 1 as a potential pharmacological target in cancer therapy, Front. Endocrinol. 3 (2013) 184.

[6] M. Chartier, M. Desgagné, M. Sousbie, C. Rumsby, L. Chevillard, L. Théroux, L. Haroune, J. Côte, J.-M. Longpré, P.-L. Boundreault, E. Marsault, P. Sarret, Pharmacodynamic and pharmacokinetic profiles of a neurotensin receptor type 2 (NTS2) analgesic macrocyclic analog, Biomed. Pharmacother. 141 (2021), 111861.

[7] W.C. Mustain, P.G. Rychahou, B.M. Evers, The role of neurotensin in physiologic and pathologic processes, Curr. Opin. Endocrinol. Diabetes Obes. 18 (2011) 75–82.

[8] M. Boules, Z. Li, K. Smith, P. Fredrickson, E. Richelson, Diverse roles of neurotensin agonists in the central nervous system, Front. Endocrinol. 4 (2013) 36.

[9] L.E. Schroeder, G.M. Leinninger, Role of central neurotensin in regulating feeding: implications for the development and treatment of body weight disorders, Biochim. Biophys. Acta 1864 (2018) 900–916.

[10] J. Ramirez-Virella, G.M. Leinninger, The role of central neurotensin in regulating feeding and body weight, Endocrinol 162 (2021) 1–14.

[11] P. Sarret, F. Caveller, Neurtensin and its receptors, in: Reference Module in Neuroscience and Biobehavioral Psychology, Elsevier, 2017, pp. 1–17.

[12] S. Tanganelli, T. Antonelli, M.C. Tomasini, S. Beggiato, K. Fuxe, L. Ferraro, Relevance of dopamine D_2/neurotensin NTS1 and NMDA/neurotensin NTS1 receptor interaction in psychiatric and neurodegenerative disorders, Curr. Med. Chem. 19 (2012) 304–316.

[13] M. Plach, T. Schäfer, D.O. Borroto-Escuela, D. Weikert, P. Gmeiner, K. Fuxe, K. Friedland, Differential allosteric modulation within dopamine D_2R-neurotensin NTS1R and D_2R-serotonini 5-HT_{2A}R receptor complexes gives bias to intracellular calcium signalling, Sci. Rep. 9 (2019), 16312.

[14] L. Jacobsen, P. Madsen, C. Jacobsen, M.S. Nielsen, J. Gliemann, C.M. Petersen, Activation and functional characterization of the mosaic receptor SorLA/LR11, J. Biol. Chem. 276 (2001) 22788–22796.

[15] J.H. Li, F. Sicard, M.A. Salam, M. Baek, J. LePrince, H. Vaudry, K. Kim, H.B. Kwon, J.Y. Seong, Molecular cloning and functional characterization of a type-I neurotensin receptor (NTR) and a novel NTR from the bullfrog brain, J. Mol. Endocrinol. 34 (2005) 793–807.

[16] P. Kleczkowska, A.W. Lipkowski, Neurotensin and neurotensin receptors: characteristic, structure-activity relationship and pain modulation – a review, Eur. J. Pharmacol. 716 (2013) 54–60.

[17] F. St-Gelais, M. Legault, M.-J. Bourque, P.-P. Rompré, L.-E. Trudeau, Role of calcium in neurotensin-evoked enhancement in firing in mesencephalic dopamine neurons, J. Neurosci. 24 (2004) 2566–2574.

[18] R. Cáceda, B. Kinkead, C.B. Nemeroff, Neurotensin: role in psychiatric and neurological diseases, Peptides 27 (2006) 2385–2404.

[19] M. Lazarova, A. Popatanasov, R. Klisurov, S. Stoeva, T. Pajpanova, R. Kalfin, L. Tancheva, Preventive effect of two new neurotensin analogues on Parkinson's disease rat model, J. Mol. Neurosci. 66 (2018) 552–560.

[20] M. Boules, L. Warrington, A. Fauq, D. McCormick, E. Richelson, Antiparkinson-like effects of a novel neurotensin analog in unilaterally 6-hydroxydopamine lesioned rats, Eur. J. Pharmacol. 428 (2001) 227–233.

[21] R. Carraway, S.E. Leeman, The amino acid sequence of a hypothalamic peptide, neurotensin, J. Biol. Chem. 250 (1975) 1907–1911.

[22] A.M. Sefler, J.X. He, T.K. Sawyer, K.E. Holub, D.O. Omecinsky, M.D. Reily, V. Thanabal, H.C. Akunne, W.L. Cody, Design and structure-activity relationships of C-terminal cyclic neurotensin fragment analogs, J. Med. Chem. 38 (1995) 249–257.

[23] K.P. Kokko, M.K. Hadden, K.L. Price, K.S. Orwig, R.E. See, T.A. Dix, In vivo behavioral effects of stable, receptor-selective neurotensin[8-13] analogues that cross the blood-brain barrier, Neuropharmacology 48 (2008) 417–425.

[24] M. Keller, K.K. Kuhn, J. Einsiedel, H. Hübner, S. Biselli, C. Mollereau, D. Wifling, J. Svobodova, G. Bernhardt, C. Cabrele, P.M.L. Venderheyden, P. Gmeiner, A. Buschauer, Mimicking of arginine by functionalized N^{ω}-carbamoylated arginine as a new broadly applicable approach to labeled bioactive peptides: high affinity angiotensin, neuropeptide Y, neuropeptide FF, and neurotensin receptor ligands as examples, J. Med. Chem. 59 (2016) 1925–1945.

[25] R. Fanelli, N. Floquet, É. Besserer-Offroy, B. Delort, M. Vivancos, J.-M. Longpré, P. Renault, J. Martinez, P. Sarret, F. Cavelier, Use of molecular modeling to design selective NTS2 neurotensin analogues, J. Med. Chem. 60 (2017) 3303–3313.

[26] L. Schindler, G. Bernhardt, M. Keller, Modifications at Arg and Ile give neurotensin (8-13) derivatives with high stability and retained NTS1 receptor affinity, ACS Med. Chem. Lett. 10 (2019) 960–965.

[27] M. Keller, S.A. Mahuroof, V.H. Yee, J. Carpenter, L. Schindler, T. Littmann, A. Pegoli, H. Hübner, G. Bernhardt, P. Gmeiner, N.D. Holliday, Fluorescence labeling of neurotensin(8-13) via arginine residues gives molecular tools with high receptor affinity, ACS Med. Chem. Lett. 11 (2020) 16–22.

[28] J.B. Thomas, A.M. Giddings, R.W. Wiethe, S. Olepu, K.R. Warner, P. Sarret, L. Gendron, J.-M. Longpre, Y. Zhang, S.P. Runyon, B.P. Gilmour, Identification of *N*-[(5-{[(4-methylphenyl)sulfonyl]amino}-3-(trifluoroacetyl)-1*H*-indol-1-yl) acetyl]-*L*-leucine (NTRC-824), a neurotensin-like nonpeptide compound selective for the neurotensin receptor type 2, J. Med. Chem. 57 (2014) 7472–7477.

[29] P. Kitabgi, F. De Nadai, C. Rovére, J.N. Bidard, Biosynthesis, maturation, release, and degradation of neurotensin and neuromedin N, Ann. N. Y. Acad. Sci. 668 (1992) 30–42.

[30] M. Sousbie, M. Vivancos, R.L. Brouillette, É. Besserer-Offroy, J.-M. Longpré, R. Leduc, P. Sarret, É. Marsault, Structural optimization and characterization of potent analgesic macrocyclic analogues of neurotensin (8-13), J. Med. Chem. 61 (2018) 7103–7115.

[31] M. Chartier, M. Desgagné, M. Sousbie, J. Côté, J.-M. Longpré, E. Marsault, P. Sarret, Design, structural optimization, and characterization of the first selective macrocyclic neurotensin receptor type 2 non-opioid analgesic, J. Med. Chem. 64 (2021) 2110–2124.

[32] I. Dubuc, P. Sarret, C. Labbé-Jullié, J.-M. Botto, E. Honoré, E. Bourdei, J. Martinez, J. Costentin, J.-P. Vincent, P. Kitagbi, J. Mazella, Identification of the receptor subtype involved in the analgesic effect of neurotensin, J. Neurosci. 19 (1999) 503–510.

[33] R. Fanelli, N. Floquet, É. Besserer-Offroy, A. Rene, J. Côté, P. Tétreault, J. Collerette-Tremblay, J.-M. Longpré, R. Leduc, J. Martinez, P. Sarret, F. Cavelier, Synthesis and characterization in vitro and in vivo of (L)-(trimethylsilyl)alanine containing neurotensin analogues, J. Med. Chem. 58 (2015) 7785–7795.

[34] F. Bumbak, T. Thomas, B.J. Noonan-Williams, T.M. Vaid, F. Yan, A.R. Whitehead, S. Bruell, M. Kocan, X. Tan, M.A. Johnson, R.A.D. Bethgate, D.K. Chalmers, P. R. Gooley, D.J. Scott, Conformational changes in tyrosine 11 of neurotensin are required to activate the neurotensin receptor 1, ACS Pharmacol. Transl. Sci. 3 (2020) 690–705.

[35] C. Devader, S. Béraud-Dufour, T. Coppola, J. Mazella, The anti-apoptotic role of neurotensin, Cells 2 (2013) 124–135.

[36] K.-E. Choi, C.L. Hall, J.-M. Sun, L. Wei, O. Mohamad, T.A. Dix, S.P. Yu, A novel stroke therapy of pharmacologically induced hypothermia after focal cerebral ischemia in mice, Faseb. J. 26 (2012) 2799–2810.

[37] J. Einsiedel, C. Held, M. Hervet, M. Plomer, N. Tschammer, H. Hübner, P. Gmeiner, Discovery of highly potent and neurotensin receptor 2 selective neurotensin mimetics, J. Med. Chem. 54 (2011) 2915–2923.

[38] C. Schaab, R.C. Kling, J. Einsiedel, H. Hübner, T. Clark, D. Seebach, P. Gmeiner, Structure-based evolution of subtype-selective neurotensin receptor ligands, ChemistryOpen 3 (2014) 206–218.

[39] A. Popatansov, S. Stoeva, M. Lazarova, L. Traikov, T. Pajpanova, R. Kalfin, L. Tancheva, Effects of new neurotensin analogue on brain activity in rat Parkinson's disease model, Bulg. Chem. Commun. Special Issue E (2017) 146–150.

[40] S. Michailova, T. Dzimbova, K. Kalíkova, E. Tesařová, T. Pajpanova, Chemical stability of new neurotensin (8-13) analogues, Bulg. Chem. Commun. Special Issue E (2017) 113–117.

[41] T. Pajpanova, S. Stoev, E. Golovinsky, G.-J. Krauß, J. Miersch, Canavanine derivatives useful in peptide synthesis, Amino Acids 12 (1997) 191–204.

[42] J.F. White, N. Noinaj, Y. Shibata, J. Love, B. Kloos, F. Xu, J. Gvozdenovic-Jeremic, P. Shah, J. Shiloach, C.G. Tate, R. Grisshammer, Structure of the agonist-bound neurotensin receptor, Nature 490 (2012) 508–513.

[43] P. Egloff, M. Hillenbrand, C. Klenk, A. Batyuk, P. Heine, S. Balada, K. M. Schlinkmann, D.J. Scott, M. Schütz, A. Plückthun, Structure of signaling-competent neurotensin Receptor 1 obtained by directed evolution in *Escherichia Coli*, Proc. Natl. Acad. Sci. U. S. A 111 (2014) E655−E662.

[44] B.E. Krumm, S. Lee, S. Bhattacharya, I. Botos, C.F. White, H. Du, N. Vaidehi, R. Grisshammer, Structure and dynamics of a constitutively active neurotensin receptor, Sci. Rep. 6 (2016), 38564.

[45] M. Delugi, A. Klipp, C. Klenk, L. Merklinger, S.A. Eberle, L. Morstein, P. Heine, P. E. Mitti, P. Ernst, T.M. Kamenecka, Y. He, S. Vacca, P. Egloff, A. Honegger, A. Plückthun, Complexes of the neurotensin receptor 1 with small-molecule ligands reveal structural determinants of full, partial, and inverse agonism, Sci. Adv. 7 (2021), eabe5504.

[46] H.E. Kato, Y. Zhang, H. Hu, C.-M. Suomivuori, F.M.N. Kadji, J. Aoki, K.K. Kumar, R. Fonseca, D. Hilger, W. Huang, N.R. Latorraca, A. Inoue, R.O. Dror, B.K. Kobilka, G. Skiniotis, Conformational transitions of a neurotensin receptor 1 – G_{i1} complex, Nature 572 (2019) 80–85.

[47] W. Yin, Z. Li, M. Jin, Y.L. Yin, P.W. de Waal, K. Pal, Y. Yin, X. Gao, Y. He, J. Gao, X. Wang, Y. Zhang, H. Zhou, K. Melcher, Y. Jiang, Y. Cong, X.E. Zhou, X. Yu, H. E. Xu, A Complex structure of arrestin-2 bound to a G protein-coupled receptor, Cell Res. 29 (2019) 971–983.

[48] W. Huang, M. Masureel, Q. Qu, J. Janetzko, A. Inoue, H.E. Kato, M.J. Robertson, K. C. Nguyen, J.S. Glenn, G. Skiniotis, B.K. Kobilka, Structure of the neurotensin receptor 1 in complex with β-arrestin 1, Nature 579 (2020) 303–308.

[49] SeeSAR package, Version 9.2 from BioSolveIT GmbH, St. Augustin, 2019. Germany, http://www.biosolveit.de/SeeSAR.

[50] T. Kühl, A. Wißbrock, N. Goradia, N. Sahoo, K. Galler, U. Neugebauer, J. Popp, S. H. Heinemann, O. Ohlenschläger, D. Imhof, Analysis of Fe(III) heme binding to cysteine-containing heme-regulatory motifs in proteins, ACS Chem. Biol. 8 (2013) 1785–1793.

[51] H.H. Brewitz, T. Kühl, N. Goradia, K. Galler, J. Popp, U. Neugebauer, O. Ohlenschläger, D. Imhof, Role of the chemical environment beyond the coordination site: structural insight into Fe(III) protoporphyrin binding to cysteine-based heme-regulatory protein motifs, Chembiochem 16 (2015) 2216–2224.

[52] E. Krieger, G. Vriend, YASARA View - molecular graphics for all devices - from smartphones to workstations, Bioinformatics 30 (2014) 2981–2982.

[53] TURBOMOLE V7.5, A Development of University of Karlsruhe and Forschungszentrum Karlsruhe GmbH, 1989-2007, TURBOMOLE GmbH, since 2007, 2020 available from: https://www.turbomole.org (TURBOMOLE GmbH).
[54] R. Ahlrichs, M. Bär, M. Häser, H. Horn, C. Kölmel, Electronic structure calculations on workstation computers: the program system turbomole, Chem. Phys. Lett. 162 (1989) 165–169.
[55] S.G. Balasubramani, G.P. Chen, S. Coriani, M. Diedenhofen, M.S. Frank, Y. J. Franzke, F. Furche, R. Grotjahn, M.E. Harding, C. Hättig, A. Hellweg, B. Helmich-Paris, C. Holzer, U. Huniar, M. Kaupp, A. Marefat Khah, S. Karbalaei Khani, T. Müller, F. Mack, B.D. Nguyen, S.M. Parker, E. Perlt, D. Rappoport, K. Reiter, S. Roy, M. Rückert, G. Schmitz, M. Sierka, E. Tapavicza, D.P. Tew, C. van Wüllen, V.K. Voora, F. Weigend, A. Wodyński, J.M. Yu, TURBOMOLE: modular program suite for *ab initio* quantum-chemical and condensed-matter simulations, J. Chem. Phys. 152 (2020), 184107.
[56] A. Schäfer, C. Huber, R. Ahlrichs, Fully optimized contracted Gaussian basis sets of triple zeta valence quality for atoms Li to Kr, J. Chem. Phys. 100 (1994) 5829–5835.
[57] A. Klamt, G. Schüürmann, COSMO: a new approach to dielectric screening in solvents with explicit expressions for the screening energy and its gradient, J. Chem. Soc., Perkin Trans. 2 (1993) 799–805.
[58] K. Baldridge, A. Klamt, First principles implementation of solvent effects without outlying charge error, J. Chem. Phys. 106 (1997) 6622–6633.
[59] A. Schäfer, A. Klamt, D. Sattel, J.C.W. Lohrenz, F. Eckert, COSMO Implementation in TURBOMOLE: extension of an efficient quantum chemical code towards liquid systems, Phys. Chem. Chem. Phys. 2 (2000) 2187–2193.
[60] H. Hübner, C. Haubmann, W. Utz, P. Gmeiner, Conjugated enynes as nonaromatic catechol bioisosteres: synthesis, binding experiments and computational studies of novel dopamine receptor agonists recognizing preferentially the D3 subtype, J. Med. Chem. 43 (2000) 756–762.
[61] R.C. Kling, C. Burchardt, J. Einsiedel, H. Huebner, P. Gmeiner, Structure-based exploration of an allosteric binding pocket in the NTS1 receptor using bitopic NT (8-13) derivatives and molecular-dynamics simulations, J. Mol. Model. 25 (2019) 193.
[62] N.A. Simeth, M. Bause, M. Dobmeier, R.C. Kling, D. Lachmann, H. Hübner, J. Einsiedel, P. Gmeiner, NTS2-selective neurotensin mimetics with tetrahydrofuran amino acids, Bioorg. Med. Chem. 25 (2017) 350–359.
[63] C. Schärfer, T. Schulz-Gasch, J. Hert, L. Heinzerling, B. Schulz, T. Inhester, M. Stahl, M. Rarey, CONFECT: conformations from an expert collection of torsion patterns, ChemMedChem 8 (2013) 1690–1700.
[64] C. Schärfer, T. Schulz-Gasch, H.C. Ehrlich, W. Guba, M. Rarey, M. Stahl, Torsion angle preferences in drug-like chemical space: a comprehensive guide, J. Med. Chem. 56 (2013) 2016–2028.
[65] (a) I. Reulecke, G. Lange, J. Albrecht, R. Klein, M. Rarey, Towards an integrated description of hydrogen bonding and dehydration: decreasing false positives in virtual screening with the HYDE scoring function, ChemMedChem 3 (6) (2008) 885–897;
(b) N. Schneider, S. Hindle, G. Lange, R. Klein, J. Albrecht, H. Briem, K. Beyer, H. Claußen, M. Gastreich, C. Lemmen, M. Rarey, Substantial improvements in large-scale redocking and screening using the novel HYDE scoring function, J. Comput. Aided Mol. Des. 12 (2012) 701–723 (and references therein).
[66] TorsionAnalyzer was Developed in Collaboration between F. Hoffmann-LaRoche, Switzerland, and the Center for Bioinformatics (ZBH) of the University of Hamburg; http://www.biosolveit.de/TorsionAnalyzer/.
[67] N.T. Tzvetkov, H.-G. Stammler, M.G. Georgieva, D. Russo, I. Faraone, A. A. Balacheva, S. Hristova, A.G. Atanasov, L. Milella, M. Antonov, M. Gastreich, Carboxamides vs. methanimines: crystal structures, binding interactions, photophysical studies, and biological evaluation of (indazole-5-yl)methanimines as monoamine oxidase B and acetylcholinesterase inhibitors, Eur. J. Med. Chem. 179 (2019) 404–422.
[68] N.T. Tzvetkov, L. Antonov, Subnanomolar indazole-5-carboxamide inhibitors of monoamine oxidase B (MAO-B) continued: indications of iron binding, experimental evidence for optimized solubility and brain penetration, J. Enzym. Inhib. Med. Chem. 32 (2017) 960–967.
[69] N.T. Tzvetkov, H.-G. Stammler, B. Neumann, S. Hristova, L. Antonov, M. Gastreich, Crytsal structures, binding interactions, and MADE evaluation of brain penetrant *N*-substituted indazole-5-carboxamides as subnanomolar, selective monoamine oxidase B and dual MAO-A/V inhibitors, Eur. J. Med. Chem. 127 (2017) 470–492.
[70] X. Chen, A. Murawski, K. Patel, C.L. Crespi, P.V. Balimane, A novel design of artificial membrane for improving the PAMPA model, Pharm. Res. (N. Y.) 25 (2008) 1511–1520.
[71] L. Di, E.H. Kerns, K. Fan, O.J. McConnell, G.T. Carter, High throughput artificial membrane permeability assay for blood-brain barrier, Eur. J. Med. Chem. 38 (2003) 223–232.
[72] P. Petkova-Kirova, A. Rakovska, G. Zaekova, C. Ballini, L.D. Corte, R. Radomirov, A. Vágvölgyi, Stimulation by neurotensin of dopamine and 5-hydroxytryptamine (5-HT) release from rat prefrontal cortex: possible role of NTR1 receptors in neuropsychiatric disorders, Neurochem. Int. 53 (2008) 355–361.
[73] H. Haga, K. Matsuo, Y. Yabuki, C. Zhang, F. Han, K. Fukunaga, Enhancement of ATP production ameliorates motor and cognitive impairments in a mouse model of MPTP-induced Parkinson's disease, Neurochem. Int. 129 (2019), 104492.
[74] R. M. Jarvik, R. Kopp, An improved one-trial passive avoidance learning situation Psychol. Rep. 21 (1967) 221–224.
[75] M. Lazarova, L. Tancheva, A. Alexandrova, E. Tsvetanova, A. Georgieva, M. Stefanova, D. Tsekova, L. Vezenkov, R. Kalfin, M. Uzunova, P. Petkova-Kirova, Effects of new galanthamine derivatives in a scopolamine model of dementia in mice, J. Alzheimer's Dis. 84 (2021) 671–690.
[76] A. Aartsma-Rus, M. van Rutten, Assessing functional performance in the Mdx mouse model, J. Vis. Exp. 85 (2014), e51303.
[77] M. Mohanasundari, M.S. Srinivasan, S. Sethupathy, M. Sabesan, Enhanced neuroprotective effect by combination of bromocripine and *Hypericum perforatum* extract against MPTP-induced neurotoxicity in mice, J. Neurobiol. Sci. 249 (2006) 140–144.
[78] H. Birla, S.N. Rai, S.S. Singh, W. Zahra, A. Rawat, N. Tiwari, R.K. Singh, A. Pathak, S.P. Singh, *Tinospora cordifola* suppresses neuroinflammation in Parkinsonian mouse model, NeuroMolecular Med. 21 (2019) 42–43.
[79] P. Chonpathompikunlert, P. Boonruamkaew, W. Sukketsiri, P. Hutamekalin, M. Sroyraya, The antioxidant and neurochemical activity of *Apium graveolens L.* and its ameliorative effect on MPTP-induced Parkinson-like symptoms in mice, BMC Compl. Alternative Med. 18 (2018) 103.
[80] P. Heimer, A.A. Tietze, C.A. Baüml, A. Resemann, F.J. Mayer, D. Suckau, O. Ohlenschläger, D. Tietze, D. Imhof, Conformational μ-conotoxin PIIIA isomers revisited: impact of cysteine pairing on disulfide-bond assignment and structure elucidation, Anal. Chem. 90 (2018) 3321–3327.
[81] O.H. Lowry, N.J. Rosebrough, A.L. Farr, R.J. Randall, Protein measurement with the folin phenol reagent, J. Biol. Chem. 193 (1951) 265–275.
[82] Y.-C. Cheng, W.H. Prusoff, Relationship between the inhibition constant (K_i) and the concentration of inhibitor which causes 50 per cent inhibition (IC_{50}) of an enzymatic reaction, Biochem. Pharmacol. 22 (1973) 3099–3108.
[83] K G. Paxinos, K. Franklin, Paxinos and Franklin's the Mouse Brain in Stereotaxic Coordinates, fifth ed., Academic Press, 2019.

Abbreviations used

ADME-T: absorption, distribution, metabolism, excretion, and toxicity
BBB: blood-brain barrier
CNS: central nervous system
DA: dopamine
DQF-COSY: double quantum filled correlation spectroscopy
DIEA (or DIPEA): N,N-diisopropylethylamine
DMF: N,N-dimethylformamide
DMSO: dimethyl sulfoxide
FBS: fetal bovine serum
Fmoc: N-(9-fluorenyl)-methoxycarbonyl
GIT: gastrointestinal tract
GPCR: G protein-coupled receptor
HBTU: 2-(1-*H*-benzotriazol-1-yl)-1,1,3,3-tetramethyluronium hexafluorophosphonate
HOBt: hydroxybenzotriazole
HYDE: hydrogen desolvation
IL: initial latency
LC-MS: liquid chromatography mass spectrometry
MPTP: 1-methyl-4-phenyl-1,2,3,6-tetrahydropyridine
MRM: multiple reaction monitoring
NOESY: nuclear Overhauser effect spectroscopy
NT: neurotensin
NT(8–13): neurotensin sequence 8-13
NTSRs: neurotensin receptors
NTS1R: neurotensin type 1 receptor
NTS2R: neurotensin type 2 receptor
6-OHDA: 6-hydroxydopamine
PAMPA: parallel artificial membrane permeability assay
PBS: phosphate-buffered saline
PD: Parkinson's disease
PPB: plasma protein binding
RP-HPLC: reversed-phase high-performance liquid chromatography
SAR: structure-activity relationship
SN: substantia nigra
SPPS: solid-phase peptide synthesis
STL: step-through latency
TFA: trifluoroacetic acid
TH: tyrosine hydroxylase
TLC: thin layer chromatography
TOCSY: total correlation spectroscopy
Vps10p: vacuolar protein sorting 10 protein
VTA: ventral tegmental area